

Article

Adaptive Control of Fuel Cell Converter Based on a New Hamiltonian Energy Function for Stabilizing the DC Bus in DC Microgrid Applications

Phatiphat Thounthong ^{1,2,*} , Pongsiri Mungporn ^{1,3} , Serge Pierfederici ⁴,
Damien Guilbert ^{5,*}  and Nicu Bizon ^{6,*} 

¹ Renewable Energy Research Centre (RERC), King Mongkut's University of Technology North Bangkok, 1518, Pracharat 1 Road, Wongsawang, Bangsue, Bangkok 10800, Thailand; pongsiri.m@tfii.kmutnb.ac.th

² Department of Teacher Training in Electrical Engineering, Faculty of Technical Education, King Mongkut's University of Technology North Bangkok, 1518, Pracharat 1 Road, Bangsue, Bangkok 10800, Thailand

³ Thai-French Innovation Institute, King Mongkut's University of Technology North Bangkok, 1518, Pracharat 1 Road, Bangsue, Bangkok 10800, Thailand

⁴ Laboratoire d'Énergétique et de Mécanique Théorique et Appliquée (LEMETA), Université de Lorraine, CNRS, LEMETA, F-54000 Nancy, France; serge.pierfederici@univ-lorraine.fr

⁵ Groupe de Recherche en Energie Electrique de Nancy (GREEN), Université de Lorraine, GREEN, F-54000 Nancy, France

⁶ Department of Electronics, Computers and Electrical Engineering, Faculty of Electronics, Communications and Computers, University of Pitesti, 1 Targul din Vale, 110040 Pitesti, Romania

* Correspondence: phatiphat.t@fte.kmutnb.ac.th (P.T.); damien.guilbert@univ-lorraine.fr (D.G.); nicu.bizon@upit.ro (N.B.)

Received: 10 October 2020; Accepted: 11 November 2020; Published: 15 November 2020



Abstract: DC microgrid applications include electric vehicle systems, shipboard power systems, and More Electric Aircraft (MEA), which produce power at a low voltage level. Rapid developments in hydrogen fuel cell (FC) energy have extended the applications of multi-phase parallel interleaved step-up converters in stabilizing DC bus voltage. The cascade architecture of power converters in DC microgrids may lead to large oscillation and even risks of instability given that the load converters considered as loads feature constant power load (CPL) characteristics. In this article, the output DC bus voltage stabilization and the current sharing of a multi-phase parallel interleaved FC boost converter is presented. The extended Port-Hamiltonian (pH) form has been proposed with the robust controller by adding an integrator action based on the Lyapunov–Energy function, named “Adaptive Hamiltonian PI controller”. The stability and robustness of the designed controller have been estimated by using Mathematica and Matlab/Simulink environments and successfully authenticated by performing experimental results in the laboratory. The results have been obtained using a 2.5 kW prototype FC converter (by two-phase parallel interleaved boost converters) with a dSPACE MicroLabBox platform. The FC main source system is based on a fuel reformer engine that transforms fuel methanol and water into hydrogen gas H_2 to a polymer electrolyte membrane FC stack (50 V, 2.5 kW).

Keywords: constant power load (CPL); microgrid; multiphase interleaved step-up converter; fuel cell (FC); Lyapunov-energy function; proportional-integral (PI) controller; Port-Hamiltonian (pH); Interconnection and Damping Assignment Passivity-Based Controller (IDA-PBC)

1. Introduction

Polymer electrolyte membrane fuel cell (PEMFC) is a sustainable source of clean and efficient energy production for the present and future generations. It has the advantages of high energy density

and high power generation efficiency, which is appropriate for DC microgrids applied to the fields of stationary as well as mobility [1,2]. Because of the electrical characteristics of FCs, low-voltage, high-current (power) converters are required to interface an FC and DC microgrid. A classical step-up converter is frequently employed as an FC converter [3,4]. Nonetheless, the operation of classical boost converters is limited when increasing the load power. For this reason, when paralleling power converters with interleaving techniques, it can offer better performance [5,6].

Present trends point out that worldwide electricity distribution systems are undergoing a transformation to direct current (DC) power transmission at both the consumption and generation level to face AC power transmission issues [4]. Moreover, renewable energy sources can operate either in DC by their operation or include a DC bus configuration where they are interfaced with power electronics, as shown in Figure 1, including electric loads, fuel cells, photovoltaic, wind turbines, or batteries [7,8]. Consequently, by employing dedicated DC distribution networks where the sources are interfaced with DC-DC converters, they enable enhancing the power quality and energy efficiency by reducing the number of power conditioning stages [9,10]. Generally, these types of distribution networks feature improved reliability compared to AC configurations given that the number of active elements included in DC/DC converters is smaller than in DC/AC converters. On the other side, another benefit of employing DC configuration is the control design since it is less complex because there are no reported issues with synchronization or no harmonic and reactive power flows [11,12].

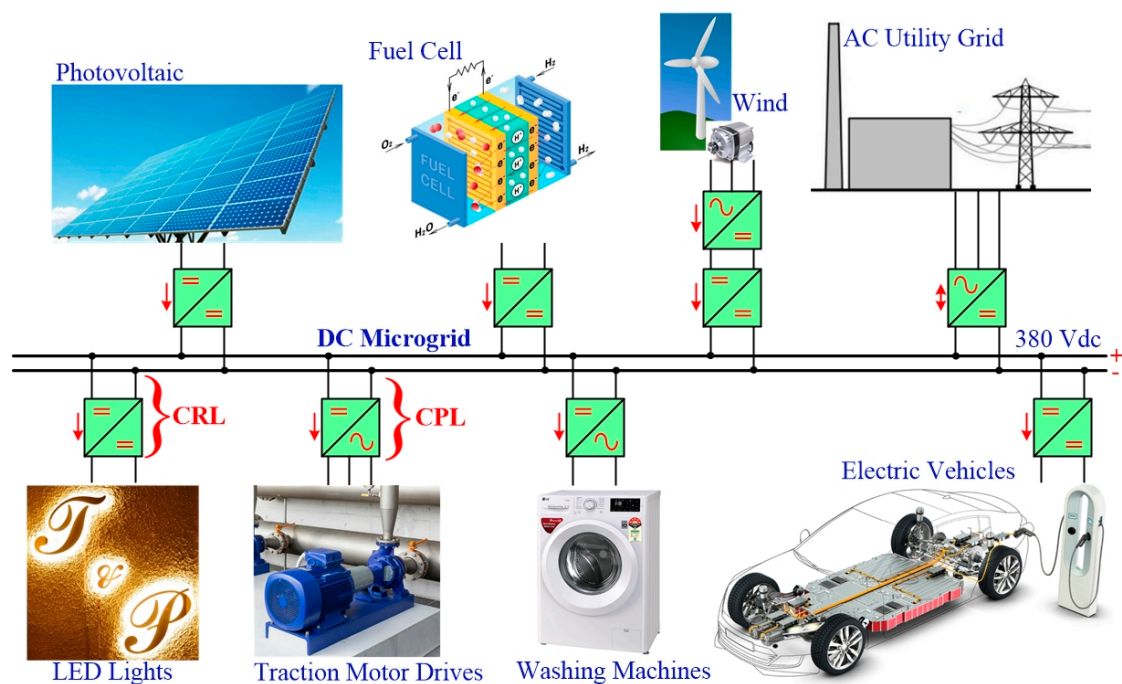


Figure 1. Future direct current (DC) microgrids.

The different loads and power sources are interconnected to the DC bus with power electronics. The different loads cannot be studied as basic impedances [i.e., constant resistive loads (CRLs)] but as constant power loads (CPLs). Given that several loads are interconnected with the DC bus through power electronics operating in closed-loop control, many of them correspond to the category of CPLs. For instance, the speed setpoint of an electric motor drive or servo drive is controlled with accuracy through feedback control loops or the charging current setpoint of an electric vehicle charger [13,14]—see Figure 1. The CPL in the DC power transmission (DC microgrid) is basically to electric vehicles, More Electric Aircrafts (MEA), spaceships, marine systems, or as power networks in residential and commercial networks. The CPL features positive instantaneous impedance but includes negative incremental impedance, which generates an oscillation phenomenon. This behavior leads to the

closed-loop network going into feedback, showing large oscillations and consequently creating instability at the DC bus output. Besides, the CPL influences system reliability and power quality [15,16]. Hence, the stabilizing control techniques studied must guarantee large-signal stability. Hence, stability has been widely investigated in DC microgrids with CPLs and several stabilization techniques have been studied and implemented: Sliding mode control for stabilizing DC-link [17]; On-line self-tuning of contouring control [18]; a frequency-dependent virtual impedance [19]; a Passivity-Based Control (PBC) through Euler-Lagrange System (ELS) [20]; a Cubature Kalman Filter Approach [21]; an energy shaping control [22]; a differential flatness approach [23], a PID Passivity-Based Control [24] and Interconnection and Damping Assignment Passivity-Based Control (IDA-PBC) [25,26]. Currently, one of the most common methods of solving the CPL complex issue is by IDA-PBC or Port-Hamiltonian Control (PCH).

In the nonlinear control technique, the PCH algorithm, characterized by a geometric approach of the DC microgrid system, has gained considerable attention from researchers [27,28]. The main features of this nonlinear control are that the DC microgrid network is considered a Port-Hamiltonian (pH) structure and the Hamiltonian function which is related to the Lyapunov function for asymptotic stability purposes. Considering the pH system, it is helpful to describe it as network models of physical components from the energy transfer in its environment via ports point of view [29,30].

In this article, a new IDA-PBC is proposed as a control algorithm for controlling an FC converter. The first version of the IDA-PBC (Hamiltonian Energy Control Law) for the 2-phase parallel interleaved boost converters (FC converter) was first presented by Mungporn et al. [31]. However, there are two main contributions to this work:

1. An integrator action is added in the extended FC converter model to guarantee that there is no error in the DC bus voltage. This means in the previous work [31] that there are three differential equations (three state variables), while in this work, there are four differential equations (four state variables).
2. The controller gain K_j (it will be presented later) has been fixed at a constant number (tuning gain) in [31]; but in this work, K_j is the real-time adaptive number (optimum gain), so that it is estimated every sampling period.

This article is structured as follows. The DC microgrid model and problem formulation are presented in Section 2. A description of the Hamiltonian energy control principle is provided in Section 3. Then, the modeling of the multi-phase parallel boost converter cells in pH structure, the new robust and adaptive control strategy, and stability proof is detailed in Section 4. Afterward, in Section 5, the obtained simulation and experimental results are introduced and discussed. Finally, Section 6 summarizes the main obtained results and discusses future prospects.

2. DC Microgrid Model and Problem Formulation

2.1. Model of Multi-Phase Boost Converter/DC Microgrid

The circuit schematic of the multi-phase parallel interleaved FC boost converters supplying an external load current i_{CH} is depicted in Figure 2. In this work, $i_{CH} \in \mathcal{R} > 0$. With the notion that the converter operates in continuous conduction mode (CCM), the well-known ordinary differential equations in the average model form [31,32] with the studied 2-phase converters ($N = 2$) are given by

$$L_1 \frac{di_{L1}}{dt} = v_{FC} - r_{L1}i_{L1} - v_C + d_1 v_C, \quad (1)$$

$$L_2 \frac{di_{L2}}{dt} = v_{FC} - r_{L2}i_{L2} - v_C + d_2 v_C, \quad (2)$$

$$C_B \frac{dv_C}{dt} = (1 - d_1)i_{L1} + (1 - d_2)i_{L2} - i_{CH}, \quad (3)$$

where i_{L1} and $i_{L2} \in \mathcal{R} > 0$ are the 1st and 2nd inductor currents [A]; $v_{FC} \in \mathcal{R} > 0$ is the FC input voltage [V]; $v_C \in \mathcal{R} > v_{FC}$ is the DC bus output voltage [V]; and d_1 and $d_2 \in [0, 1]$ are the 1st and 2nd duty

cycles [pu.] of the switch S_1 and S_2 (the shift between the PWM gate control signals is of 180° out of phase); L_1 and L_2 are the 1st and 2nd inductances [H]; C_B is the DC bus capacitance [F]; and r_{L1} and r_{L2} are the equivalent series resistance (ESR) [Ω] in the inductance L_1 and L_2 and also represent static losses in each converter cell.

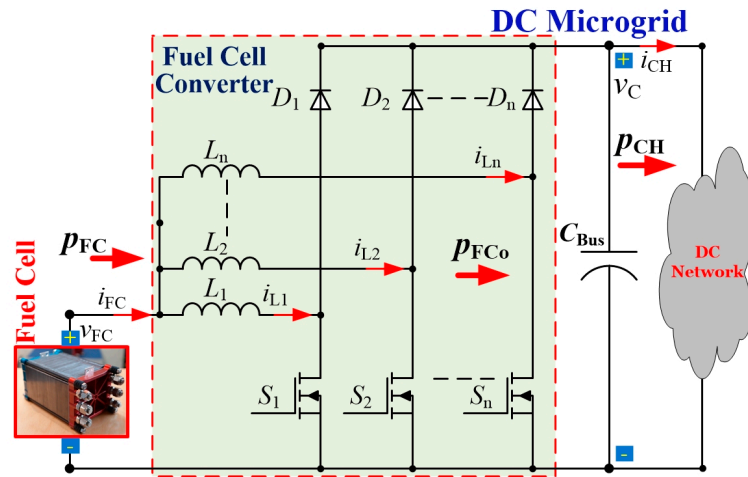


Figure 2. Multiphase parallel step-up converters for fuel cell (FC) main source in DC microgrid applications.

There are 2 types of load characteristics in the DC microgrid, see Figure 1. The first one is the constant resistive load CRL. It can be expressed as

$$i_{CH} = \frac{v_C}{R_{CH}}, \tag{4}$$

where R_{CH} is the constant resistive load [Ω]. The second one is the constant power load CPL. It can also be expressed as

$$i_{CH} = \frac{p_{CH}}{v_C}, \tag{5}$$

where p_{CH} is the constant power load (W) and one may define $p_{CH} = p_{CPL}$. As shown in Figure 3, the CPL features positive spontaneous impedance but also a negative incremental impedance. Despite the spontaneous impedance ($v_C/i_{CH} > 0$) of the CPL being positive, the change in the impedance ($\Delta v_C/\Delta i_{CH} < 0$) is negative. This may lead to large oscillation or instability of the DC bus voltage. The instability due to negative impedance can be explained with a simple example. A basic approach to studying the stability of a system is through a small-signal Eigenvalue analysis. For the system model (1)–(3) and simplification that $i_L = i_{L1} = i_{L2}$; $i_{FC} = 2i_L$; $r = r_{L1} = r_{L2}$; $d = d_1 = d_2$; and $L = L_1 = L_2$, one may write

$$L \frac{di_{FC}}{dt} = 2v_{FC} - r_L i_{FC} - 2v_C + 2dv_C, \tag{6}$$

$$C_B \frac{dv_C}{dt} = i_{FC} - di_{FC} - i_{CH}. \tag{7}$$

The linearized model ($x = X + \tilde{x}$) of (6) and (7) [33,34] can be expressed in the s -domain by taking the Laplace transform as

$$Ls\tilde{i}_{FC}(s) = 2\tilde{v}_{FC}(s) - r_L\tilde{i}_{FC}(s) - 2\tilde{v}_C(s) + 2D\tilde{v}_C(s) + 2V_C\tilde{d}(s), \tag{8}$$

$$C_B s\tilde{v}_C(s) = \tilde{i}_{FC}(s) - D\tilde{i}_{FC}(s) - I_{FC}\tilde{d}(s) - \tilde{i}_{CH}(s), \tag{9}$$

where D , V_C , and I_{FC} are the linearized operating point. The characteristic Equation of (8) and (9) is

$$LC_B s^2 + \left[r_L C_B + \frac{L}{R_{CH}} \right] s + \left[\frac{r_L}{R_{CH}} + 2(1 - D)^2 \right] = 0. \tag{10}$$

Referring to (5), the negative incremental impedance R_{CPL} can be expressed as

$$R_{CPL} = -\frac{v_C^2}{P_{CPL}}. \tag{11}$$

Then, from (10) and (11), the needed conditions to keep the system pole at the left half plane for the stability constraint can be illustrated by

$$P_{CPL} < \frac{r_L C_B V_C^2}{L}. \tag{12}$$

Referring to (6) and (7) and for stability conditions for 2-phase boost converters, one may summarize here that for CRL:

$$P_{CH} < \frac{v_{FC}^2}{2r_L} = P_{FCMax}. \tag{13}$$

For the CPL, one may write

$$P_{CH} < \min\left(\frac{r_L C_B V_C^2}{L}, \frac{v_{FC}^2}{2r_L}\right). \tag{14}$$

According to (6) at the equilibrium point, the open-loop control of the FC boost converter, the duty cycle (control signal d_{OP}), can be expressed as

$$d_{OP} = \frac{v_{Cd} - v_{FC} + r_L \cdot i_L}{v_C}, \tag{15}$$

where v_{Cd} is the desired DC bus voltage set-point. It can be simplified as

$$d_{OP} = \frac{v_{Cd} - v_{FC}}{v_C}. \tag{16}$$

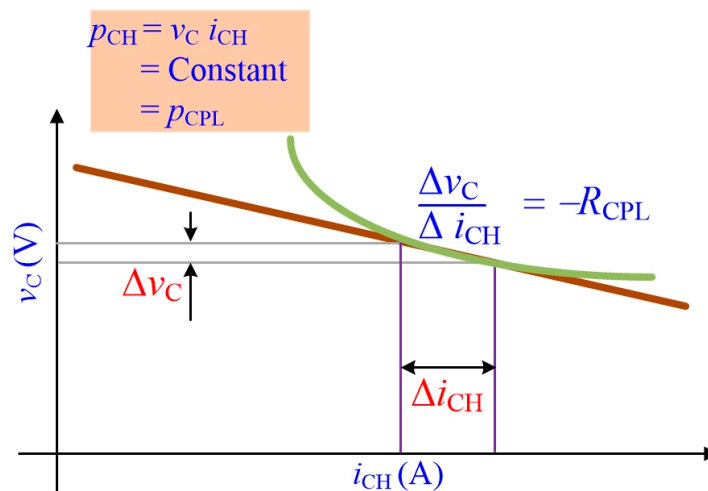


Figure 3. Negative incremental impedance behavior of constant power load (CPL) in DC microgrid; the DC output voltage decreases with an increase in load current.

2.2. The FC Boost Converter Characteristics under CRL or CPL

Simulation results for the FC boost converter (2-phase) in open-loop control (presented above in Section 2.1) were obtained using the switching model realized in the Matlab/Simulink environment. The FC converter parameters are the real parameters. They can be seen in Table A1. The simulation results under CRL are shown in Figures 4 and 5. In Figure 4, CH1–CH4 are the DC bus voltage v_C , load power p_{CH} , FC current i_{FC} , and first duty cycle d_1 (note $d = d_1 = d_2$), respectively. By comparison, in Figure 4, at time = 2 ms, the FC boost converter is subjected to pure CRL step (the final power from 2500 W to 3200 W) to which a small oscillation and stability are observed at the DC bus output voltage. Moreover, given that the 2-phase FC boost converter is included in the plane, it is conceivable to achieve a comprehensive picture of the characteristic of the converter in open-loop by drawing their phase space (or phase plot): v_C vs. i_{FC} ($=i_{L1} + i_{L2}$). Figure 5 illustrates the phase spaces of the converter with some pathways for different initial conditions and at $d = 0.5767$ and $v_{FC} = 50$ V. The initial conditions selected (\diamond) illustrate the steady-state points with different values for the resistive load R_{CH} . It can be highlighted that the system converges to the desiderated steady-state point ($R_{CH} = 3.78 \Omega$) for a wide range of initial conditions.

More importantly, the simulation results under CPL are shown in Figures 6 and 7. In Figure 6, CH1–CH4 are the DC bus voltage v_C , load power p_{CH} , FC current i_{FC} , and first duty cycle d_1 (note $d = d_1 = d_2$), respectively. Referring to (14) and converter parameters provided in Table A1, the critical CPL is 3025 W. In Figure 6a, at time = 5 ms, the converter is subjected to pure CPL step [the final power from 2250 W (<3025 W) to 2500 W (<3025 W)], to which a large oscillation is observed at the DC bus output voltage. Next, in Figure 6b, at time = 5 ms, the converter is subjected to pure CPL step [the final power from 2500 W (<3025 W) to 3200 W (>3025 W)] to which instability is noticeable at the DC bus output voltage. At the same time, Figure 7 depicts the phase spaces (v_C vs. i_{FC}) of the converter under the same condition of Figure 6b. It is clear that even though the FC boost converter is operated in open-loop control if the CPL is lower than the critical power (here, CPL 3025 W), the DC bus voltage creates a large oscillation and if the CPL is over the critical power, the system is unstable.

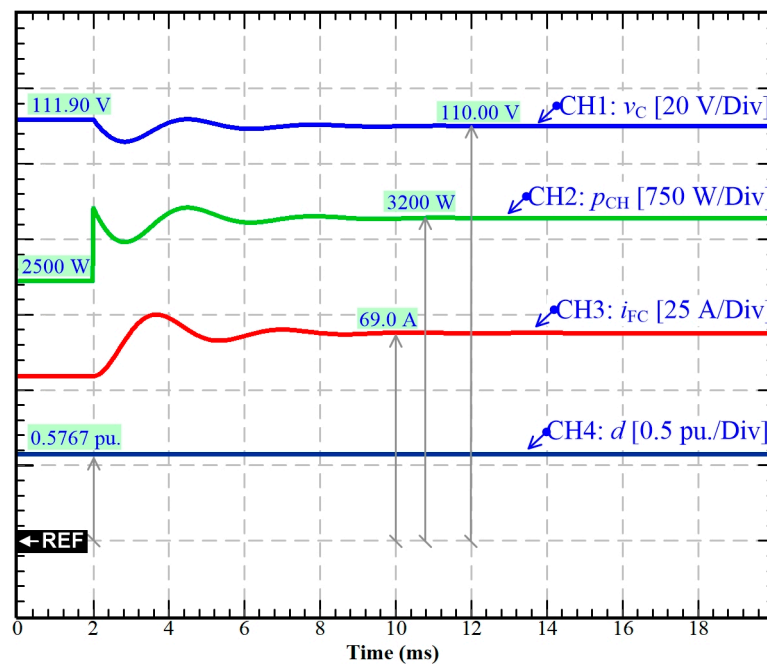


Figure 4. Simulation results: constant resistive loads (CRL) step from 5.00Ω to 3.78Ω of the 2-phase FC boost converter with the open-loop control at a constant duty cycle $d = 0.5767$ (the FC boost converter parameters are expressed in Table A1).

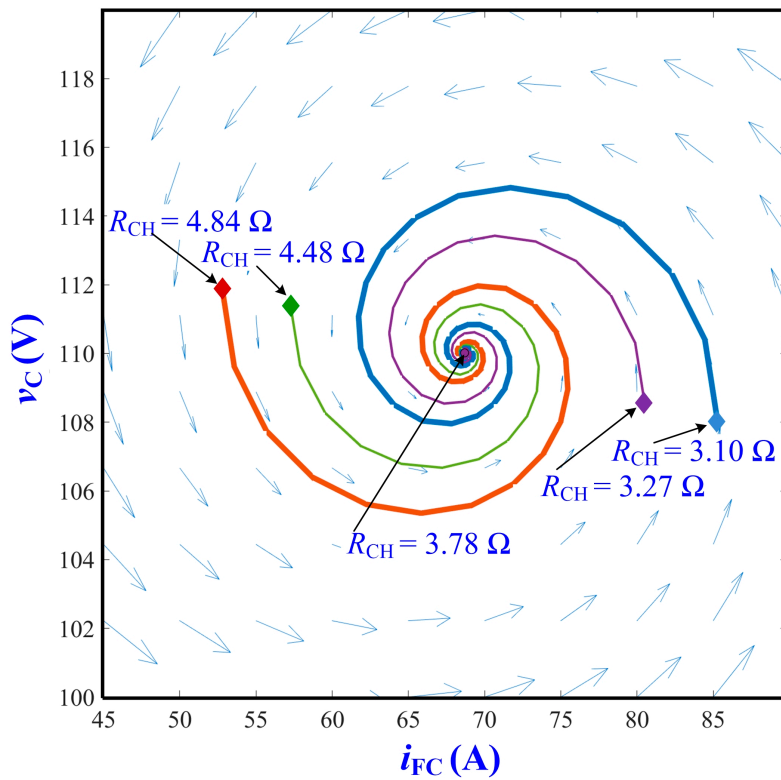


Figure 5. Phase plane (v_C vs. i_{FC}) of the 2-phase FC boost converters with the open-loop control with CRL at a constant duty cycle $d = 0.5767$ for different initial conditions of R_{CH} (the FC boost converter parameters are expressed in Table A1).

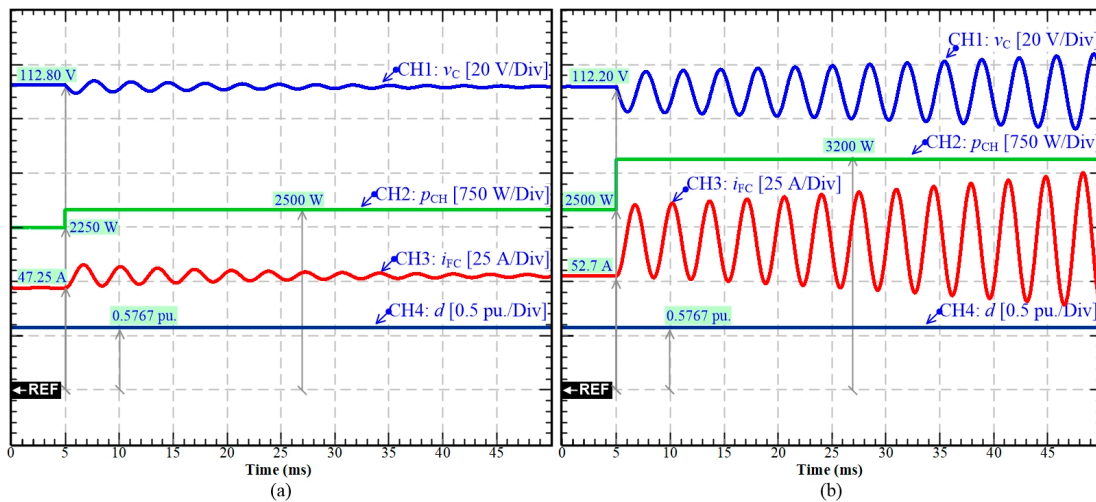


Figure 6. Simulation results: CPL step of the 2-phase FC boost converter with the open-loop control at a constant duty cycle $d = 0.5767$: (a) from 2250 W to 2500 W; (b) from 2500 W to 3200 W.

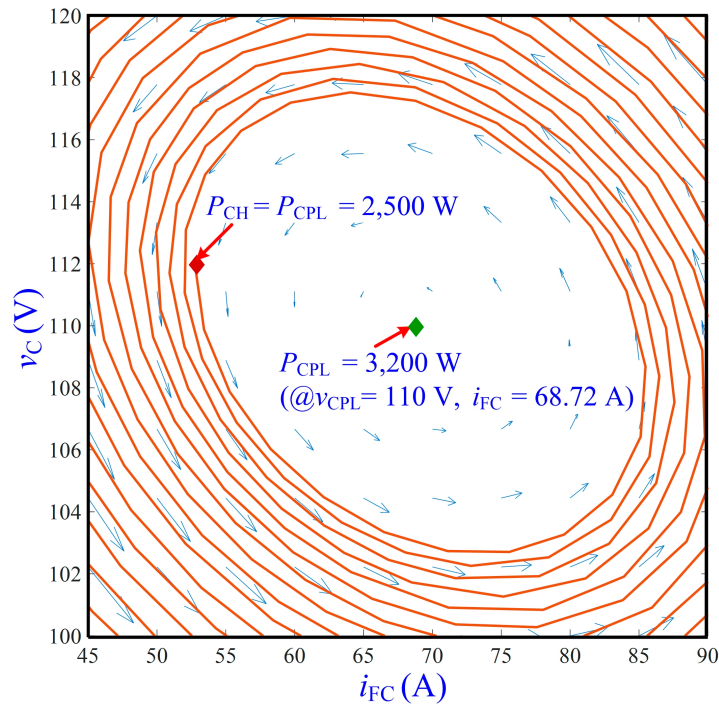


Figure 7. Phase plane (v_C vs. i_{FC}) of the FC boost converter with the open-loop control at a constant duty cycle $d = 0.5767$ under CPL step from 2500 W to 3200 W, instability case.

3. Hamiltonian Control Theory

3.1. Model of Port-Hamiltonian (pH)

A non-linear system [35,36] can be given by:

$$\dot{\mathbf{x}} = \mathbf{f}(\mathbf{x}) + \mathbf{g}(\mathbf{x}) \cdot \mathbf{u} + \boldsymbol{\xi}. \tag{17}$$

Then, it can be rewritten as a pH form [37,38] as follows:

$$\dot{\mathbf{x}} = [\mathbf{J}(\mathbf{x}) - \mathbf{R}(\mathbf{x})] \frac{\partial H(\mathbf{x})}{\partial \mathbf{x}} + \mathbf{g}(\mathbf{x}) \cdot \mathbf{u} + \boldsymbol{\xi}, \tag{18}$$

where $\mathbf{x} \in \mathcal{R}^n$ is the state vector, $\mathbf{u} \in \mathcal{R}^m$ ($m \leq n$) is the input or control vector, $\mathbf{J}(\mathbf{x}) = -\mathbf{J}(\mathbf{x})^T \in \mathcal{R}^{n \times n}$ is the interconnection matrix (or the skew symmetric matrix), $\mathbf{R}(\mathbf{x}) = \mathbf{R}(\mathbf{x})^T \geq 0 \in \mathcal{R}^{n \times n}$ is the damping matrix (or the dissipation symmetric matrix or the positive-definite matrix), $H(\mathbf{x})$ is the Hamiltonian function (or the energy function), $\mathbf{g}(\mathbf{x}) \in \mathcal{R}^{n \times m}$ is the input matrix, and $\boldsymbol{\xi} \in \mathcal{R}^n$ is the external or disturbance vector.

3.2. Hamiltonian Energy Control Law

The Hamiltonian energy control or the Interconnection and Damping Assignment Passivity-Based Controller (IDA-PBC) is a control technique proposed in [31,39], which enables one to design a feedback loop which is a closed-loop system, which can be seen as the Hamiltonian form

$$\dot{\mathbf{x}} = [\mathbf{J}_d(\mathbf{x}) - \mathbf{R}_d(\mathbf{x})] \frac{\partial H_d(\mathbf{x})}{\partial \mathbf{x}} + \frac{d\mathbf{x}_d}{dt}, \tag{19}$$

where $\mathbf{J}_d(\mathbf{x}) = -\mathbf{J}_d(\mathbf{x})^T$ is the desired control interconnection matrix, $\mathbf{R}_d(\mathbf{x}) = \mathbf{R}_d(\mathbf{x})^T \geq 0$ is the desired control damping matrix, and $H_d(\mathbf{x})$ is the desired Hamiltonian function (or the desired energy function), also known as the *Lyapunov* function, needs to fulfill

$$x_d = \operatorname{argmin}(H_d), \tag{20}$$

where x_d is the desired steady-state point.

By substituting (19) into (18) and using mathematical manipulations, the following matching equation is expressed as:

$$\overbrace{[\mathbf{J}_d(\mathbf{x}) - \mathbf{R}_d(\mathbf{x})] \frac{\partial H_d(\mathbf{x})}{\partial \mathbf{x}} + \frac{dx_d}{dt}}^{\text{Control Law}} = \overbrace{[\mathbf{J}(\mathbf{x}) - \mathbf{R}(\mathbf{x})] \frac{\partial H(\mathbf{x})}{\partial \mathbf{x}} + \mathbf{g}(\mathbf{x}) \cdot \mathbf{u} + \boldsymbol{\xi}}^{\text{Plant}}, \tag{21}$$

when equality (21) is solved for the control signals \mathbf{u} , the control signals are finally obtained

$$\mathbf{u} = \beta(x). \tag{22}$$

4. Hamiltonian Energy Control of Fuel Cell Converter

4.1. Multi-Phase Parallel FC Boost Converter Model in pH Form

According to (1)–(3) (the studied two-phase FC boost converters), the state variables and the control variables are defined as

$$\mathbf{x} = [x_1 \ x_2 \ x_3]^T = [i_{L1} \ i_{L2} \ v_C]^T \text{ and } \mathbf{u} = [u_1 \ u_2]^T = [d_1 \ d_2]^T. \tag{23}$$

Refer to the standard pH form (18), the positive-definite diagonal matrix \mathbf{Q} is defined as

$$\mathbf{Q} = \begin{bmatrix} L_1 & 0 & 0 \\ 0 & L_2 & 0 \\ 0 & 0 & C_B \end{bmatrix}. \tag{24}$$

Then, the Hamiltonian function $H(\mathbf{x})$ (or the total stored energy) can be expressed as

$$H(\mathbf{x}) = \frac{1}{2} \mathbf{x}^T \mathbf{Q} \mathbf{x} = \frac{1}{2} (L_1 x_1^2 + L_2 x_2^2 + C_B x_3^2). \tag{25}$$

Arrangement of the gradient of $H(\mathbf{x})$ with respect to \mathbf{x} can be determined as

$$\frac{\partial H(\mathbf{x})}{\partial \mathbf{x}} = [L_1 x_1 \ L_2 x_2 \ C_B x_3]^T. \tag{26}$$

Therefore, the 2-phase FC boost converters in the standard pH form can be represented as

$$\underbrace{\begin{bmatrix} \dot{x}_1 \\ \dot{x}_2 \\ \dot{x}_3 \end{bmatrix}}_{\dot{\mathbf{x}}} = \underbrace{\begin{bmatrix} -\frac{r_L}{L^2} & 0 & -\frac{1}{LC_B} \\ 0 & -\frac{r_L}{L^2} & -\frac{1}{LC_B} \\ \frac{1}{LC_B} & \frac{1}{LC_B} & 0 \end{bmatrix}}_{\mathbf{J-R}} \underbrace{\begin{bmatrix} Lx_1 \\ Lx_2 \\ C_B x_3 \end{bmatrix}}_{\frac{\partial H(\mathbf{x})}{\partial \mathbf{x}}} + \underbrace{\begin{bmatrix} \frac{x_3}{L} & 0 \\ 0 & \frac{x_3}{L} \\ -\frac{x_1}{C_B} & -\frac{x_2}{C_B} \end{bmatrix}}_{\mathbf{g}(\mathbf{x})} \underbrace{\begin{bmatrix} u_1 \\ u_2 \end{bmatrix}}_{\mathbf{u}} + \underbrace{\begin{bmatrix} \frac{v_{FC}}{L} \\ \frac{v_{FC}}{L} \\ -\frac{i_{CH}}{C_B} \end{bmatrix}}_{\boldsymbol{\xi}}, \tag{27}$$

with the simplification that $r = r_{L1} = r_{L2}$ and $L = L_1 = L_2$.

4.2. Extended FC Boost Converters Model in pH Form

The most essential variable in the DC microgrid is the DC bus voltage v_C . Therefore, the first key objective is to control $v_C = v_{Cd}$ (=a desired DC bus voltage set-point). According to the well-known control strategy (21) based on the IDA-PBC approach, the control system (21) may feature static errors because of the effects of model errors, uncertainties, and noise. Consequently, the integral action is added to solve this issue and to enhance the performance of the control strategy. At this point, a new variable λ is defined as

$$\lambda = K_I \int (v_{Cd} - v_C) dt, \tag{28}$$

where K_I is the tuning controller gain (or the integral gain).

Refer to (27), the extended FC converter model with the added integrator action (28) can be expressed in pH form with the new extended state vector x :

$$x = [x_1 \ x_2 \ x_3 \ x_4]^T = [i_{L1} \ i_{L2} \ v_C \ \lambda]^T. \tag{29}$$

The extended Hamiltonian function (or the total energy) in the quadratic form is defined as

$$H(x) = \frac{1}{2} x^T Q_E x, \tag{30}$$

$$\text{with } Q_E = [L_1 \ L_2 \ C_B \ 1/K_I]^T. \tag{31}$$

Then,

$$H(x) = \frac{1}{2} (L_1 x_1^2 + L_2 x_2^2 + C_B x_3^2 + K_I^{-1} x_4^2). \tag{32}$$

After that, the gradient of $H(x)$ with respect to x can be defined as

$$\frac{\partial H(x)}{\partial x} = [L_1 x_1 \ L_2 x_2 \ C_B x_3 \ K_I^{-1} x_4]^T. \tag{33}$$

Finally, the extended 2-phase FC boost converters model in the standard pH form can be represented as

$$\underbrace{\begin{bmatrix} \dot{x}_1 \\ \dot{x}_2 \\ \dot{x}_3 \\ \dot{x}_4 \end{bmatrix}}_{\dot{x}} = \underbrace{\begin{bmatrix} -\frac{r_L}{L^2} & 0 & -\frac{1}{LC_B} & 0 \\ 0 & -\frac{r_L}{L^2} & -\frac{1}{LC_B} & 0 \\ \frac{1}{LC_B} & \frac{1}{LC_B} & 0 & 0 \\ 0 & 0 & -\frac{K_I}{C_B} & 0 \end{bmatrix}}_{J-R} \underbrace{\begin{bmatrix} Lx_1 \\ Lx_2 \\ C_B x_3 \\ K_I^{-1} x_4 \end{bmatrix}}_{\frac{\partial H(x)}{\partial x}} + \underbrace{\begin{bmatrix} \frac{x_3}{L} & 0 \\ 0 & \frac{x_3}{L} \\ -\frac{x_1}{C_B} & -\frac{x_2}{C_B} \\ 0 & 0 \end{bmatrix}}_{g(x)} \underbrace{\begin{bmatrix} u_1 \\ u_2 \end{bmatrix}}_u + \underbrace{\begin{bmatrix} \frac{v_{FC}}{L} \\ \frac{v_{FC}}{L} \\ -\frac{i_{CH}}{C_B} \\ K_I v_{Cd} \end{bmatrix}}_{\xi}. \tag{34}$$

With $r = r_{L1} = r_{L2}$ and $L = L_1 = L_2$, $J(x)$ and $R(x)$ can be expressed as

$$J(x) = \begin{bmatrix} 0 & 0 & -\frac{1}{LC_B} & 0 \\ 0 & 0 & -\frac{1}{LC_B} & 0 \\ \frac{1}{LC_B} & \frac{1}{LC_B} & 0 & 0 \\ 0 & 0 & -\frac{K_I}{C_B} & 0 \end{bmatrix}, \tag{35}$$

$$R(x) = \begin{bmatrix} \frac{r_L}{L^2} & 0 & 0 & 0 \\ 0 & \frac{r_L}{L^2} & 0 & 0 \\ 0 & 0 & 0 & 0 \\ 0 & 0 & 0 & 0 \end{bmatrix}. \tag{36}$$

It should be noted here that $\mathbf{J}(\mathbf{x}) \neq \mathbf{J}(\mathbf{x})^T$; however, the most important condition is $\mathbf{J}_d(\mathbf{x}) = -\mathbf{J}_d(\mathbf{x})^T$ and it will be presented later in the following control law.

4.3. Proposed Adaptive Hamiltonian PI Control Law

To apply the control law described in Section 3.2, it is mandatory to define H_d , \mathbf{J}_d , and R_d . Then, the error state vector is defined as

$$\mathbf{e} = [e_1 \ e_2 \ e_3 \ e_4]^T = [(x_{1d} - x_1) \ (x_{2d} - x_2) \ (x_{3d} - x_3) \ (x_{4d} - x_4)]^T, \tag{37}$$

where x_d is the desired variable set-point. According to (30) and (31), the desired Hamiltonian energy function $H_d(x)$ is chosen as the quadratic function:

$$H_d(x) = \frac{1}{2} \mathbf{e}^T \mathbf{Q}_E \mathbf{e} = \frac{1}{2} (L_1(x_1 - x_{1d})^2 + L_2(x_2 - x_{2d})^2 + C_B(x_3 - x_{3d})^2 + K_I^{-1}(x_4 - x_{4d})^2). \tag{38}$$

Next, the gradient of $H_d(x)$ with respect to \mathbf{x} can be given as

$$\frac{\partial H_d(x)}{\partial \mathbf{x}} = [L_1(x_1 - x_{1d}) \ L_2(x_2 - x_{2d}) \ C_B(x_3 - x_{3d}) \ K_I^{-1}x_4]^T \text{ with } x_{4d} = 0. \tag{39}$$

Next, the control interconnection matrix \mathbf{J}_C is defined as

$$\mathbf{J}_C(\mathbf{x}) = \begin{bmatrix} 0 & 0 & -\frac{K_J}{LC_B} & 0 \\ 0 & 0 & -\frac{K_J}{LC_B} & 0 \\ \frac{K_J}{LC_B} & \frac{K_J}{LC_B} & 0 & \frac{K_I}{C_B} \\ 0 & 0 & 0 & 0 \end{bmatrix}, \tag{40}$$

where $K_J \in \mathcal{R}$ is the real-time adaptive controller gain and $K_I \in \mathcal{R} \geq 0$ is the integral gain [refer to (28)]. Based on the matrix $\mathbf{J}(\mathbf{x})$ in (35), the desired interconnection matrix is defined as

$$\mathbf{J}_d(\mathbf{x}) = \mathbf{J}(\mathbf{x}) + \mathbf{J}_C(\mathbf{x}) = \begin{bmatrix} 0 & 0 & -\frac{1}{LC_B} & 0 \\ 0 & 0 & -\frac{1}{LC_B} & 0 \\ \frac{1}{LC_B} & \frac{1}{LC_B} & 0 & 0 \\ 0 & 0 & -\frac{K_I}{C_B} & 0 \end{bmatrix} + \begin{bmatrix} 0 & 0 & -\frac{K_J}{LC_B} & 0 \\ 0 & 0 & -\frac{K_J}{LC_B} & 0 \\ \frac{K_J}{LC_B} & \frac{K_J}{LC_B} & 0 & \frac{K_I}{C_B} \\ 0 & 0 & 0 & 0 \end{bmatrix}, \tag{41}$$

$$\mathbf{J}_d(\mathbf{x}) = \begin{bmatrix} 0 & 0 & -\frac{(1+K_J)}{LC_B} & 0 \\ 0 & 0 & -\frac{(1+K_J)}{LC_B} & 0 \\ \frac{(1+K_J)}{LC_B} & \frac{(1+K_J)}{LC_B} & 0 & \frac{K_I}{C_B} \\ 0 & 0 & -\frac{K_I}{C_B} & 0 \end{bmatrix}, \mathbf{J}_d(\mathbf{x}) = -\mathbf{J}_d(\mathbf{x})^T. \tag{42}$$

Next, the desired damping matrix $R_d(x)$ is defined as

$$\mathbf{R}_d(\mathbf{x}) = \begin{bmatrix} \frac{K_R}{L^2} & 0 & 0 & 0 \\ 0 & \frac{K_R}{L^2} & 0 & 0 \\ 0 & 0 & 0 & 0 \\ 0 & 0 & 0 & 0 \end{bmatrix}, \tag{43}$$

where $K_R \in \mathcal{R} \geq 0$ is the tuning damping controller gain.

By substituting (34), (39), (42), and (43) into (21) and using mathematical manipulations, the following matching equation is expressed as

$$\underbrace{\begin{bmatrix} -\frac{K_R}{L^2} & 0 & -\frac{(1+K_J)}{LC_B} & 0 \\ 0 & -\frac{K_R}{L^2} & -\frac{(1+K_J)}{LC_B} & 0 \\ \frac{(1+K_J)}{LC_B} & \frac{(1+K_J)}{LC_B} & 0 & \frac{K_I}{C_B} \\ 0 & 0 & -\frac{K_I}{C_B} & 0 \end{bmatrix}}_{J_d - R_d} \underbrace{\begin{bmatrix} L(x_1 - x_{1d}) \\ L(x_2 - x_{2d}) \\ C_B(x_3 - x_{3d}) \\ K_I^{-1}x_4 \end{bmatrix}}_{\frac{\partial H_d(x)}{\partial x}} = \underbrace{\begin{bmatrix} -\frac{r_L}{L^2} & 0 & -\frac{1}{LC_B} & 0 \\ 0 & -\frac{r_L}{L^2} & -\frac{1}{LC_B} & 0 \\ \frac{1}{LC_B} & \frac{1}{LC_B} & 0 & 0 \\ 0 & 0 & -\frac{K_I}{C_B} & 0 \end{bmatrix}}_{J-R} \underbrace{\begin{bmatrix} Lx_1 \\ Lx_2 \\ C_Bx_3 \\ K_I^{-1}x_4 \end{bmatrix}}_{\frac{\partial H(x)}{\partial x}} + \underbrace{\begin{bmatrix} \frac{x_3}{L} & 0 \\ 0 & \frac{x_3}{L} \\ -\frac{x_1}{C_B} & -\frac{x_2}{C_B} \\ 0 & 0 \end{bmatrix}}_{g(x)} \underbrace{\begin{bmatrix} u_1 \\ u_2 \end{bmatrix}}_{u} + \underbrace{\begin{bmatrix} \frac{v_{FC}}{L} \\ \frac{v_{FC}}{L} \\ -\frac{i_{CH}}{C_B} \\ K_I x_{3d} \end{bmatrix}}_{\xi}. \tag{44}$$

Finally, one solves (44) and then the last bottom equation is equal to zero; there are only three (3)–Equations and three (3)–unknown variables u_1 , u_2 , and K_J to be solved with two (2) tuning controllers K_R and K_I . Besides, it is important to point out that the term $\frac{dx_d}{dt}$, which appears in Equation (21), has been set to zero so that it can be neglected in practice if the dynamic bound is slow in comparison with the other dynamics.

The unique solution can be expressed as

$$K_J = \frac{- (i_{CH}x_3 - v_{FC}x_1 - v_{FC}x_2 + x_3x_4 + x_1x_{3d} - x_3x_{1d} + x_2x_{3d} - \dots)}{x_3x_{2d} - K_Rx_1^2 - K_Rx_2^2 + r_Lx_1^2 + r_Lx_2^2 + K_Rx_1x_{1d} + K_Rx_2x_{2d}} / (x_1x_{3d} - x_3x_{1d} + x_2x_{3d} - x_3x_{2d}), \tag{45}$$

$$u_1 = \frac{x_{3d} - v_{FC} + r_Lx_1}{v_C} + \frac{K_R(x_{1d} - x_1) + K_J(x_{3d} - x_3)}{v_C}, \tag{46}$$

$$u_2 = \frac{x_{3d} - v_{FC} + r_Lx_2}{v_C} + \frac{K_R(x_{2d} - x_2) + K_J(x_{3d} - x_3)}{v_C}. \tag{47}$$

4.4. Desired Reference Generation x_d

To estimate the load power p_{CH} , one may write

$$p_{CH} = v_C i_{CH} = x_3 i_{CH}. \tag{48}$$

Referring to (28) and (29), the load power estimation from (48) can be simplified as

$$p_{CH} = x_{3d} i_{CH} + x_{3d} x_4. \tag{49}$$

Depending on its applications in the DC microgrid to the DC voltage $v_C (=x_3)$ level, the output voltage set-point x_{3d} is 270–540 V for electric vehicles [40,41], or 750 V for city tramways [42,43]; 270–350 V for the More Electric Aircraft MEA [44,45]; or 1200–6000 V for shipboard power system [46,47]. Finally, desired inductor current set-points $i_{L1d} (=x_{1d})$ and $i_{L2d} (=x_{2d})$ are assessed via (1)–(3); we set $dx/dt = 0$ and $x = x_d$ and simplify $r = r_{L1} = r_{L2}$. Then, the desired FC power reference p_{FCd} can be expressed as

$$p_{FCd} = \frac{v_{FC}^2}{r_L} \left(1 - \sqrt{1 - \frac{p_{CH}}{P_{FCmax}}} \right), \tag{50}$$

with

$$P_{FCMax} = \frac{v_{FC}^2}{2r_L} P_{FCMax} = \frac{v_{FC}^2}{2r_L}. \tag{51}$$

Then,

$$i_{FCd} = \frac{p_{FCd}}{v_{FC}}, i_{L1d} = i_{L2d} = \frac{i_{FCd}}{2}. \tag{52}$$

4.5. Stability Proof, Tuning Controller Gains, and Control Conclusion

Proof. Condition I. Consider the control law (46) and (47) in closed-loop with pH system (34) and the Lyapunov candidate function V is the desired Hamiltonian energy function $H_d(x)$ [refer to (38)]:

$$V = H_d(x), \tag{53}$$

$$V = \frac{1}{2}(L_1(x_1 - x_{1d})^2 + L_2(x_2 - x_{2d})^2 + C_B(x_3 - x_{3d})^2 + K_I^{-1}(x_4)^2)_{x_{4d}=0} > 0.$$

We can straightforwardly validate that $V > 0$ is positive definite, therefore the equilibrium point (x_{1d}, x_{2d}, x_{3d}) is stable.

Condition II. Next, it only remains to certify the asymptotic stability of the control system. Computing the derivative of V , we achieve

$$\dot{V} = \frac{dH_d(x)}{dt} = \left(\frac{\partial H_d(x)}{\partial x} \right)^T \frac{dx}{dt}, \tag{54}$$

$$\dot{V} = \left(\frac{\partial H_d(x)}{\partial x} \right)^T \left([J_d(x) - R_d(x)] \frac{\partial H_d(x)}{\partial x} \right), \tag{55}$$

=0, ($J_d = -J_d^T$)

$$\dot{V} = \left[\left(\frac{\partial H_d(x)}{\partial x} \right)^T \cdot J_d \cdot \frac{\partial H_d(x)}{\partial x} \right] - \left[\left(\frac{\partial H_d(x)}{\partial x} \right)^T \cdot R_d \cdot \frac{\partial H_d(x)}{\partial x} \right], \tag{56}$$

$$\dot{V} = - \left[\left(\frac{\partial H_d(x)}{\partial x} \right)^T R_d \frac{\partial H_d(x)}{\partial x} \right] < 0. \tag{57}$$

$R_d(x) = R_d(x)^T > 0$

The asymptotic stability in closed-loop with the pH system follows directly from the standard Lyapunov theory. So, it can be determined that the equilibrium point (x_{1d}, x_{2d}, x_{3d}) is asymptotically stable ($V > 0$ & $\dot{V} < 0$) [48,49], completing the proof. □

For tuning the controller gains, the proposed control strategy has three degrees of freedom because of H_d , J_d , and R_d ; as a result, we have only the two (2) tuned controller gains: K_R and K_I ; for K_I , it is the real-time adaptive estimation gain (45). Next, one roughly proposes a setting of a damping controller K_R :

$$K_R = (2...10) \cdot r_L. \tag{58}$$

According to the Nyquist–Shannon theorem, the relationship between the above-integral time constant ($=1/K_I$) and the boost converter’s natural frequency $\omega_n [=1/\sqrt{L C_B}]$, $L = L_1 = L_2$ is roughly expressed based on the cascade control loop:

$$K_I \ll \omega_n. \tag{59}$$

Finally, the developed control algorithm explained in the previous sections is illustrated in Figure 8. The integrator action (28) calculates x_4 and the reference generation (50) creates the desired FC power p_{FCd} . For safety reasons, p_{FCd} must be constrained in terms of its scope, i.e., within an interim [$p_{FCrated}$ (corresponding the FC rated power) and minimum FC power p_{FCmin} (set to 0 W)]. Next, the reference generations (52) estimates the desired inductor-currents i_{Ld} ($=x_{1d} = x_{2d}$); again, this signal must be constrained in terms of its scope, i.e., within an interim [rated inductor current i_{Lrated} (equivalent to an FC rated current/2 [2 phase converter cells]) and minimum inductor current i_{Lmin} (set to 0 A)]. To finish, the control vector generation (45)–(47) produces duty-cycle control variables u : d_1, d_2 . The developed adaptive Hamiltonian-energy control of the DC microgrid is given in Figure 8. According to the control law (45)–(47) and the integrator action (28) (it generates x_4), one can see that $x_{1d} = x_{2d} = f(x_4)$ and $K_J = f(x_4)$. For this reason, one may name the control law (45)–(47) “Adaptive Hamiltonian–PI Controller”.

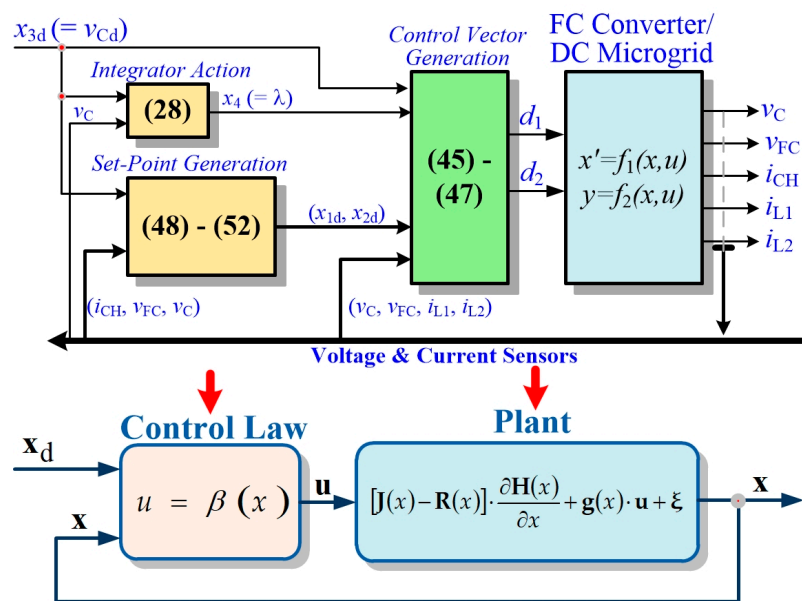


Figure 8. Proposal of the adaptive Hamiltonian energy control for an FC converter.

5. Simulation and Test Bench Results

5.1. Description of the Experimental Platform

The description of the developed experimental platform is provided in Appendix A. The experimental tests were performed in the laboratory by connecting a DC microgrid of 110 V scale loaded by the electronic loads. The oscilloscope monitor waveforms in Figure 9a,b demonstrate the switching characteristics of the interleaved parallel two-phase step-up converters at CPL = 450 W and at CPL = 1200 W, respectively. CH1–CH5 are the FC voltage v_{FC} , the load power p_{CH} , the FC current i_{FC} , the first inductor current i_{L1} , and the second inductor current i_{L2} , respectively. The currents are acquired through three current clamps where their sensitivities were set at 5 A/div (Figure 9a) and 10 A/div (Figure 9b). The obtained experimental results show that the FC current ripple is small, optimizing the reliability of the FC over a long operating period [4,5]. The FC current i_{FC} consists of the sum of both inductor currents i_{L1} and i_{L2} . The FC converter is two-phase interleaved boost converters (refer to Figure 2) where the two main power switches are shifted of $2\pi/N$ ($N = 2$) out of phase. Therefore, the inductor ripple currents allow them to compensate for each other and to reduce the FC ripple current (close to a pure DC current).

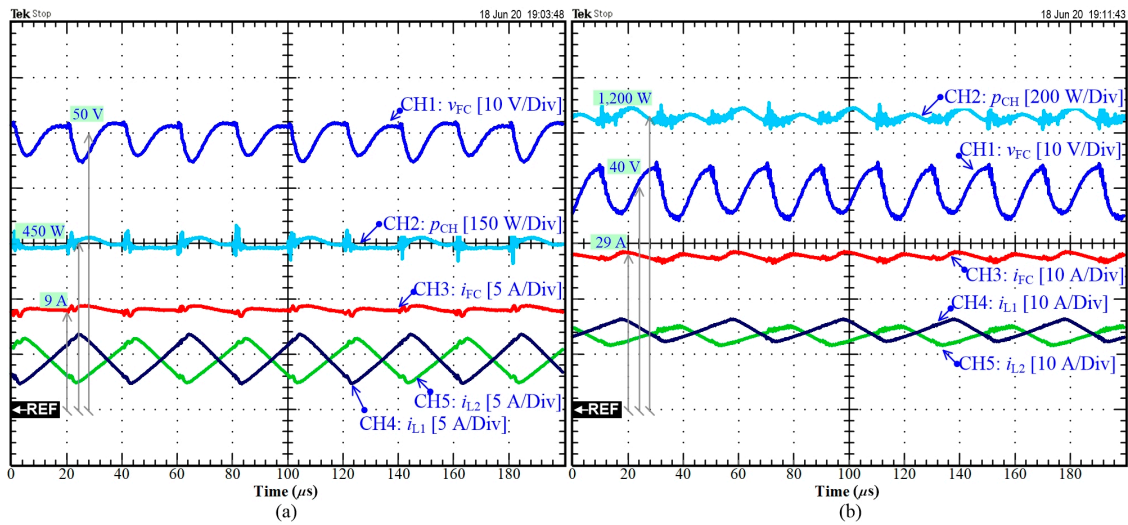


Figure 9. Experimental results: Signal waveforms of the FC converter: (a) at CPL = 450 W, (b) at CPL = 1200 W.

5.2. Obtained Simulation and Experimental Results for Static and Dynamic Operations

Then, to validate the system modeling and the design of the controllers, simulations were carried out by using MATLAB/Simulink™ environment where the switching model of the interleaved parallel two-phase boost circuits were implemented. To corroborate the DC link voltage v_C stabilization by the proposed Hamiltonian control law, the simulation and experimental results in Figure 10a,b show the system response to a large load power step (disturbance) under CPL. CH1–CH11 represent the DC link voltage v_C ($=x_3$), the FC voltage v_{FC} , the FC power p_{FC} , the load power p_{CH} , the first-inductor current i_{L1} ($=x_1$), the second-inductor current i_{L2} ($=x_2$), the first duty cycle d_1 ($=u_1$), the second duty cycle d_2 ($=u_2$), the FC current i_{FC} , the integrator action output x_4 , and the real-time adaptive gain K_J , respectively. The simulations and experimental test results illustrate similar waveforms, justifying the system modeling adopted in Section 2. The reported results show slight disturbances on the DC bus voltage signal of 110 V as a result of a step load from 160 to 840 W and the duty cycles d_1 and d_2 change to a new steady-state operating point within nearly 20 ms, which is of major significance in the application of the suggested Hamiltonian control approach. It is important to point out that an ideal CPL does not occur in practice. As emphasized previously, the firmly controlled electronic load operates similarly to the CPL. Hence, by substituting the CPL with a firmly regulated power circuit, the simulation of CPL is feasible. The CPL is achieved in this work through a controlled converter (operating as an electronic load) to supply power to a load. As displayed in Figure 10b, to speed up the stepped CPL, the controlled CPL is operated to behave as 2nd order characteristics with overshoot (underdamped). It has to be noted that the DC link voltage v_C is globally asymptotically stable during the high CPL and intelligently, i_{L1} is close to i_{L2} ; this means the input main source FC current is almost equal to 2-times the inductor current and $i_{L1} \approx i_{L2}$.

Afterward, to validate the DC bus voltage v_C balance by the proposed Hamiltonian control law under CRL, experimental results in Figure 11a,b display the system response to the large load power step (disturbance) under CRL: 48.40 Ω to 16.57 Ω (Figure 11a: positive load power transition \uparrow); and 16.57 Ω to 48.40 Ω (Figure 11b negative load power transition \downarrow). The oscilloscope channels CH1–CH11 are the same measured signals as shown in Figure 10. It can be perceived in Figure 11 that the DC bus output voltage v_C , the load power p_{CH} , the FC power p_{FC} , the FC current i_{FC} , the inductor currents i_L , and the duty cycles d settle to their desired steady-state operating point with excellent dynamic performance.

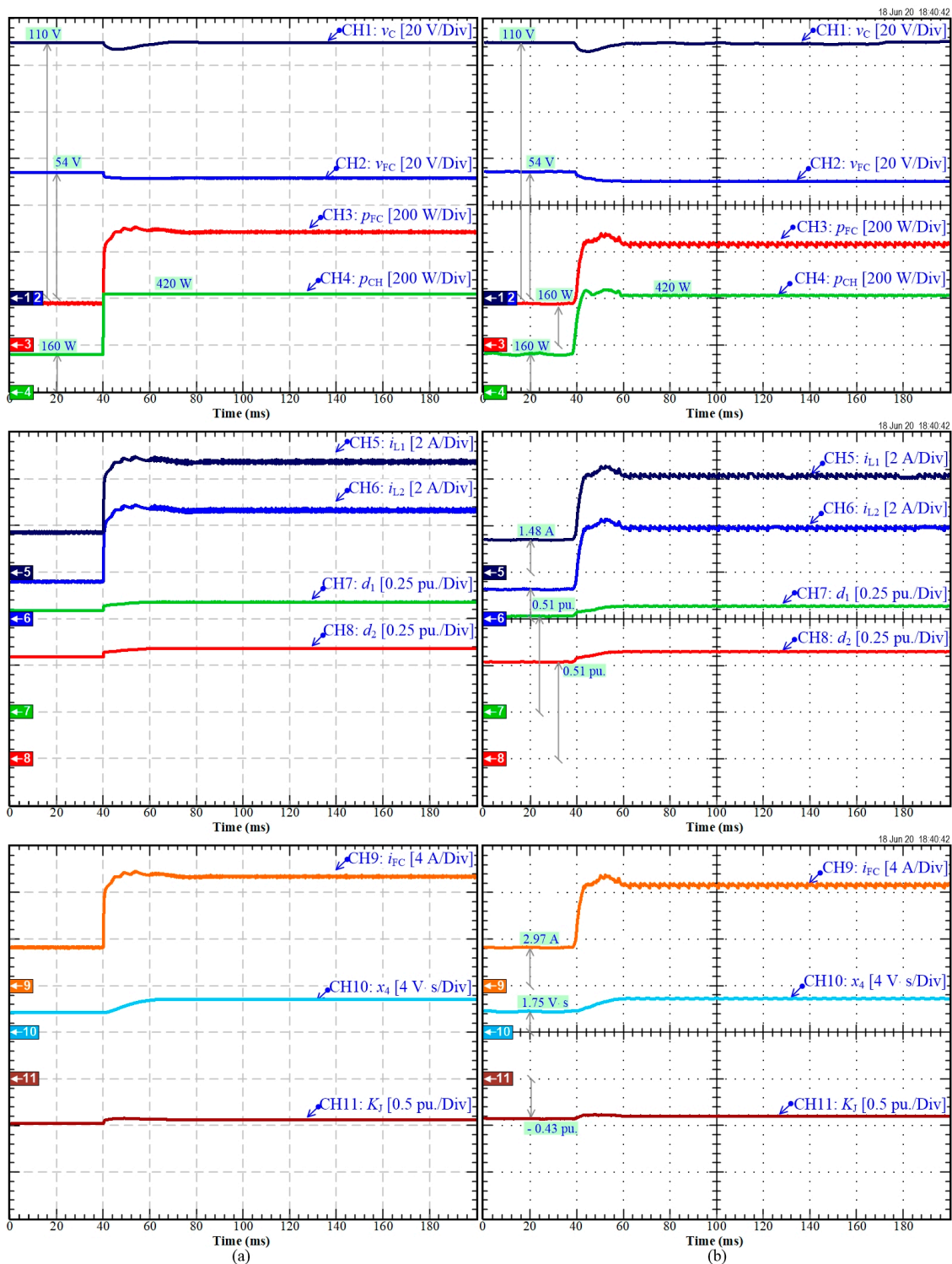


Figure 10. Dynamic characteristics of the FC converter in a CPL step from 160 to 420 W: (a) Simulation results; (b) Experimental results.

Afterwards, Figure 12 displays the signals that were acquired during a long load cycle; it shows from top to bottom: the DC bus voltage v_C , the FC voltage v_{FC} , the load power p_{CH} , the FC power p_{FC} , the FC current i_{FC} , the 1st inductor current i_{L1} , and the 1st duty cycle d_1 . These experimental results approve that the DC bus voltage v_C is asymptotically globally stable during large CPL cycles: positive power transitions \uparrow and negative power transitions \downarrow .

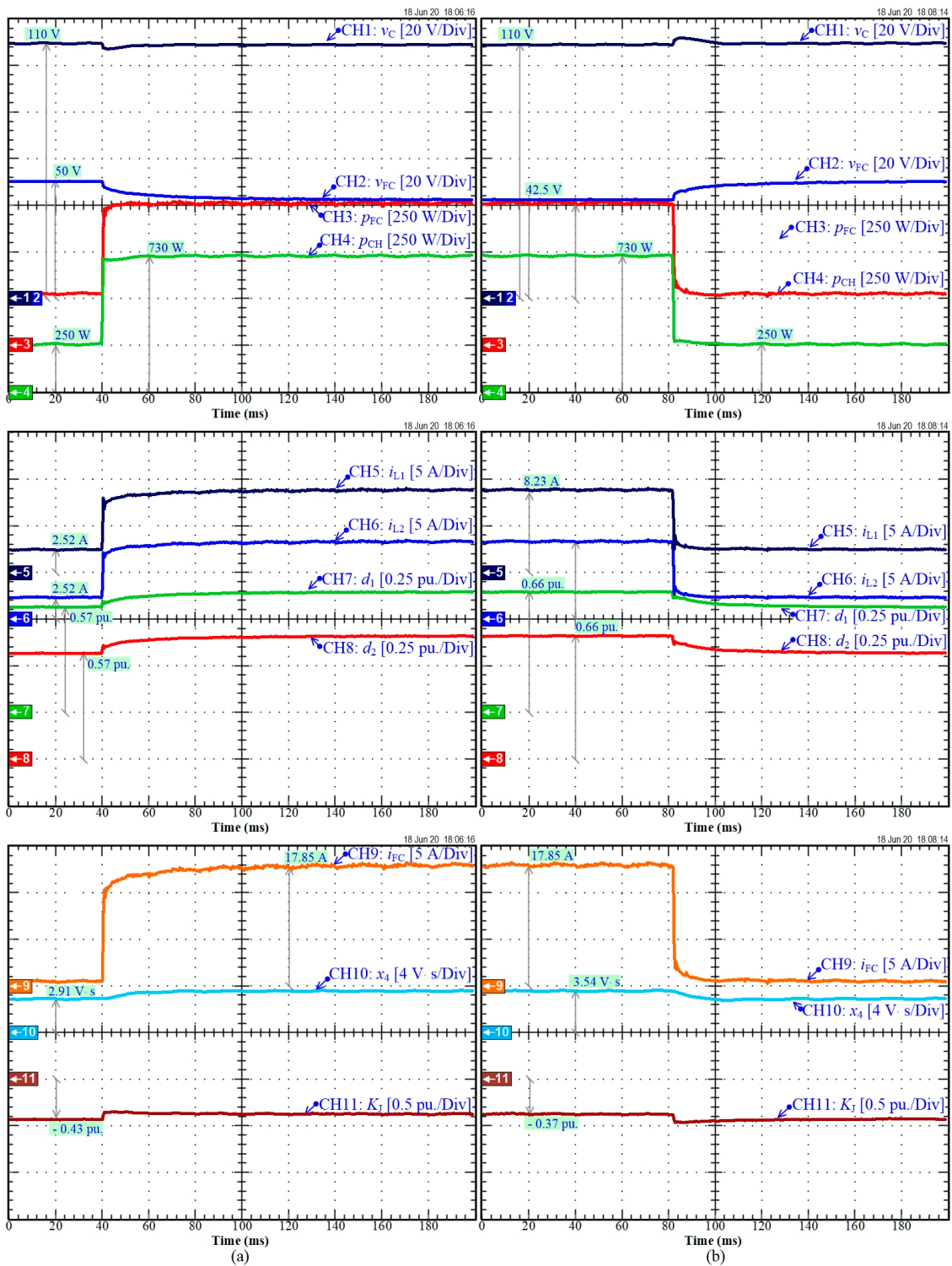


Figure 11. Experimental test bench results: Dynamic behavior of the FC converter during a CRL step: (a) 48.40 Ω to 16.57 Ω; (b) 16.57 Ω to 48.40 Ω.

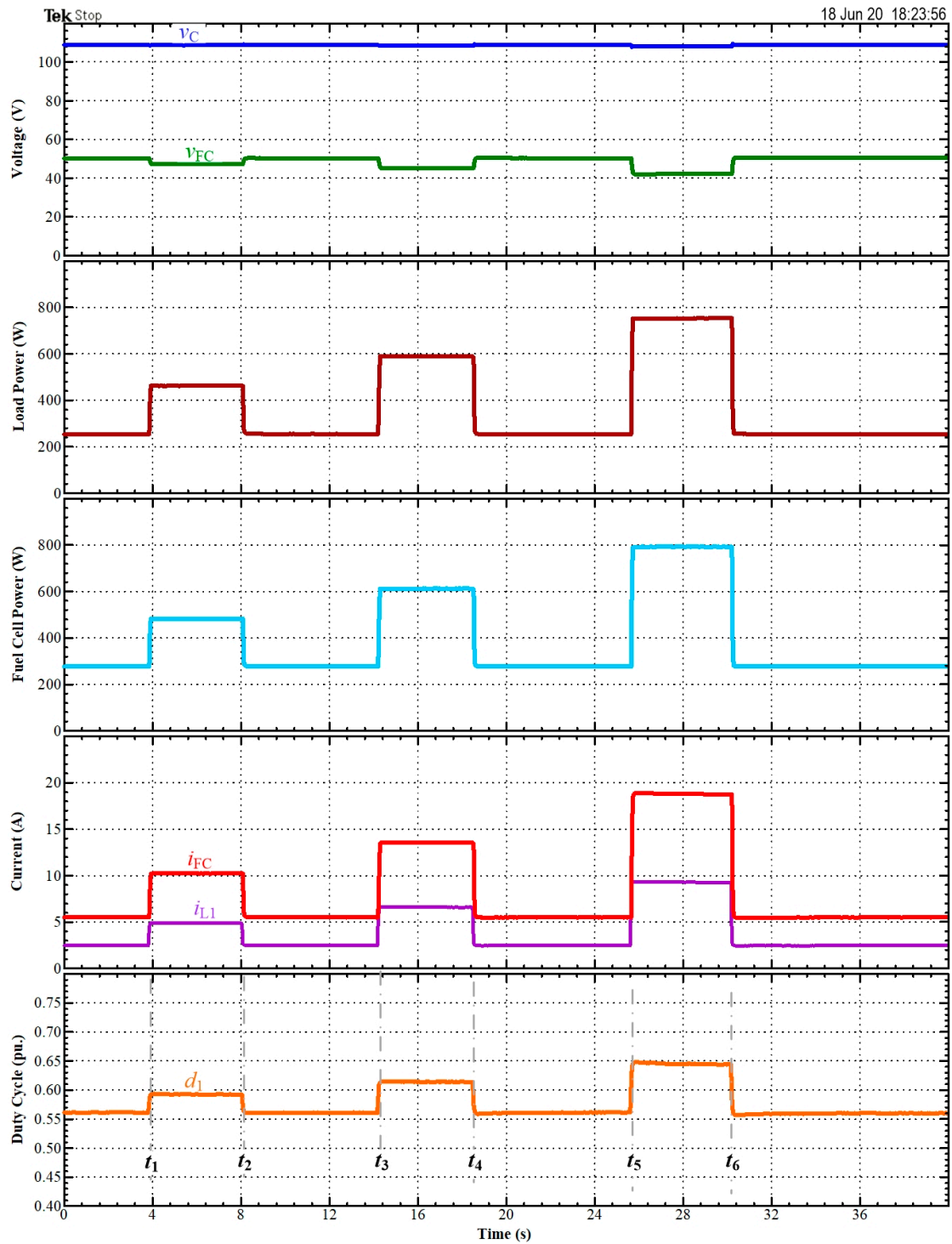


Figure 12. Experimental test bench results: FC converter response during the long load cycles.

For comparison purposes, a well-known cascade linear proportional-integral (PI) control approach is concisely detailed. The external control loop consists of DC bus voltage v_C and the internal control loops include two inductor currents i_{L1} and i_{L2} . The cascade linear PI control laws [50,51] are set by the following expressions:

$$d_1 = K_{Pi}(i_{L1d} - i_{L1}) + K_{Pi} \int_0^t (i_{L1d} - i_{L1})d\tau, \tag{60}$$

$$d_2 = K_{Pi}(i_{L2d} - i_{L2}) + K_{Ii} \int_0^t (i_{L2d} - i_{L2}) d\tau, \quad (61)$$

$$p_{FCd} = K_{Pv}(v_{Cd} - v_C) + K_{Iv} \int_0^t (v_{Cd} - v_C) d\tau, \quad (62)$$

$$\text{with } i_{L1d} = i_{L2d} = \left(\frac{p_{FCd}}{v_{FC}} \right) / 2, \quad (63)$$

where K_{Pi} , K_{Ii} , K_{Pv} , and K_{Iv} are the tuning controller parameters.

To assess the performance of the classic linear PI control law (60)–(63) and the proposed adaptive Hamiltonian PI control law, simulations have been performed through MATLAB/Simulink. The choice of PI controllers for comparison purposes is motivated by the following reasons:

1. Since a classic interleaved boost converter (including only two phases) is used in this work to interface the fuel cell and the DC bus, the transfer function of the converter can be obtained easily by using Laplace Transform.
2. The parameters of the PI controllers can be tuned to achieve the best performance by using phase margin methods as reported in the literature.
3. PI controllers are well-known in the literature and they are generally employed in the industry.
4. The development of other robust controllers (sliding mode, passivity control, fuzzy logic, Lyapunov-based controllers) would be more challenging for comparison purposes.
5. By comparing with classic PI controllers, the performance of proposed controllers can be emphasized from the stability and dynamic response point of view.

To provide a detailed and accurate comparison between both approaches, the parameters of the linear PI controllers have been tuned to gain the best performance. So, $K_{Pi} = 0.02 \text{ A}^{-1}$, $K_{Ii} = 20 \text{ A}\cdot\text{s}^{-1}$, $K_{Pv} = 30 \text{ W}\cdot\text{V}^{-1}$, and $K_{Iv} = 65,000 \text{ W}\cdot\text{V}\cdot\text{s}^{-1}$. Figures 13–15 show the simulation results obtained for both approaches during large load steps. CH1–CH4 represent the DC-bus voltage v_C , the first duty cycle d_1 , the load power p_{CH} , and the FC current i_{FC} , respectively. For the same CRL step from 6.05Ω to 4.84Ω , it is portrayed in Figure 13. The proposed adaptive Hamiltonian PI control law exhibits better dynamics of the DC bus voltage balance to its desired reference of 110 V ($=v_{Cd}$). Even though the dynamic response of the linear PI control law could be enhanced based on that illustrated in Figure 13a, this enhancement could be achieved at the expense of system stability. More importantly, the same CPL step from 2000 W to 2500 W is depicted in Figure 14. The linear PI control law exhibits large oscillation of the DC bus voltage v_{Cd} and the proposed adaptive Hamiltonian PI control law demonstrates better dynamics of the DC bus voltage balance. Finally, the critical CPL of 3025 W (refer to (12), Figures 6b and 7), is shown in Figure 15; the linear PI control law exhibits the system as unstable but the proposed adaptive Hamiltonian PI control law features excellent dynamics of the DC bus voltage balance. Based on these results, it can be concluded that the proposed adaptive Hamiltonian PI control law offers better performance and efficiency than the classic linear PI controller, particularly for the CPL applications in a DC microgrid.

5.3. Comparison of the Performances Compared to Previous Works

As emphasized in the introduction, this work is an extension of a previously published work in [31] where a control algorithm based on port-controlled Hamiltonian was applied to multiphase interleaved boost converter interfacing fuel cells and the DC bus of a microgrid. This algorithm was designed taking into consideration three state variables, both inductor currents in the multiphase interleaved boost converter and the DC bus voltage. In the case under study, to meet the issues from the static error point of view and to enhance the performance of the controller, an integral action was added and considered as a new state variable. Besides, in the proposed Hamiltonian PI control

law, the new algorithm includes an adaptive controller gain which is tuned in real-time according to the conditions (static and dynamic). By bringing these new improvements in the control law, better performance can be obtained, particularly from the stabilization of the DC bus voltage point of view. Indeed, in [31], after sudden load change, the control law takes some time to stabilize the DC bus voltage; while in the proposed work, the stabilization of the DC bus voltage is faster. Finally, for long load cycles, including several sudden load changes (direct and inverse), the reported works in [31] show oscillations and slight overshoot in DC bus voltage regulation; whereas in Figure 12, the DC bus voltage is kept constant without overshoot and oscillations despite the load change.

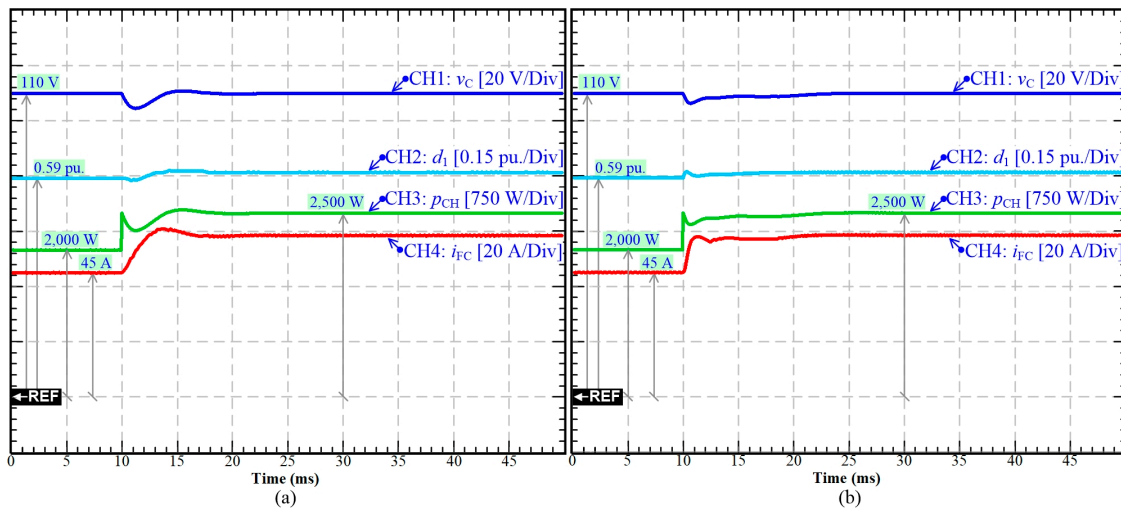


Figure 13. Simulation results: Dynamic behavior of the FC converter during a CRL step: 6.05Ω to 4.84Ω : (a) linear proportional-integral (PI) control law; (b) proposed adaptive Hamiltonian PI control law.

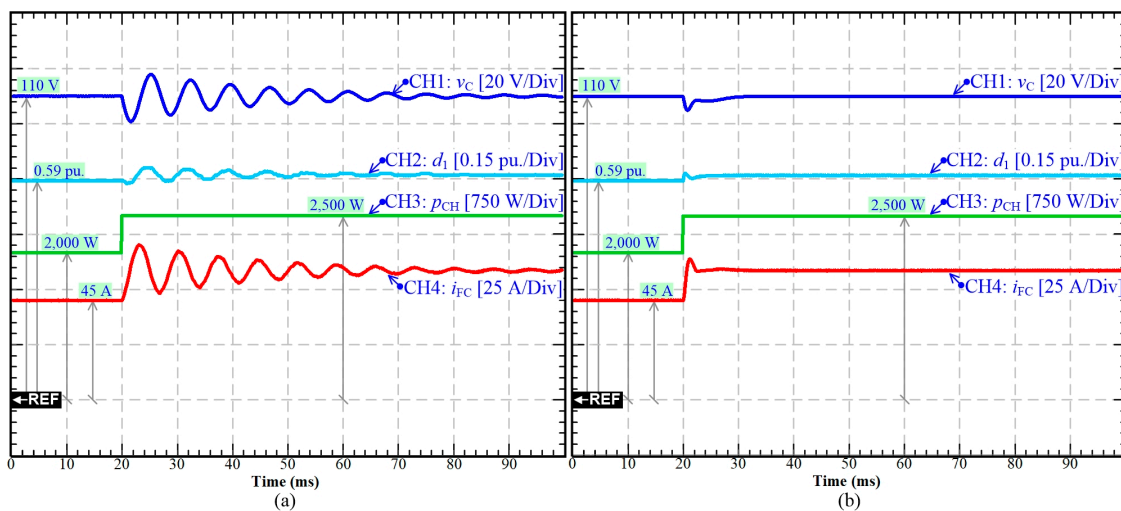


Figure 14. Simulation results: Dynamic behavior of the FC converter during a CPL step: 2000 W to 2500 W: (a) linear PI control law; (b) proposed adaptive Hamiltonian PI control law.

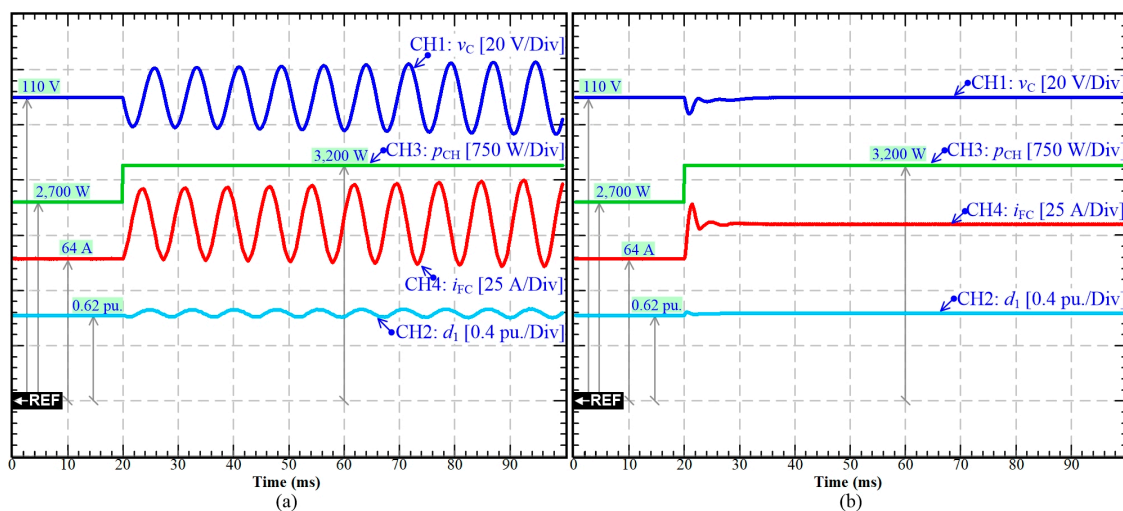


Figure 15. Simulation results: Dynamic behavior of the FC converter during a CPL step: 2700 W to 3200 W: (a) linear PI control law; (b) proposed adaptive Hamiltonian PI control law.

6. Conclusions

This article has proposed an improved control law based on the Hamiltonian Lyapunov function to balance the output DC bus voltage of multi-phase DC/DC boost converters supplying a CRL or CPL for PEMFC applications compared to the previous works. The control scheme considers that the load power is known (by using a load current sensor) and is realized through the development of an IDA-PBC that balances the output DC bus voltage. An integral action (to guarantee the DC bus voltage error = 0) has been combined to enhance the performance of the IDA-PBC approach. The system modeling and design of the controllers have been thoroughly investigated through simulations performed in the MATLAB/Simulink environment and experiments through a suitable experimental platform, demonstrating the practical feasibility of the approach. Besides, it has been demonstrated that the novel IDA-PBC algorithm features better performance in DC bus voltage stabilization (without oscillations and overshoot) despite the sudden load change (direct and indirect) in comparison with classic PI controllers (leading up to large oscillations and instability). For future works, another integral action may be considered to improve system performances. Furthermore, it would be interesting to use an improved IDA-PBC algorithm to control different sources and energy storage devices (including hydrogen storage through electrolyzer) through power electronics in a DC microgrid.

Author Contributions: Conceptualization, N.B.; methodology, S.P.; software, P.M.; validation, S.P. and D.G.; formal analysis, N.B.; investigation, N.B.; resources, P.M.; data curation, P.T.; writing—original draft preparation, P.T. and D.G.; writing—review and editing, P.T., D.G., and N.B.; visualization, N.B.; supervision, S.P.; project administration, P.T.; funding acquisition, P.T. All authors have read and agreed to the published version of the manuscript.

Funding: This work was partially supported by the International Research Partnerships: Electrical Engineering Thai-French Research Center (EE-TFRC) between Université de Lorraine (UL) and King Mongkut's University of Technology North Bangkok (KMUTNB) through the Research Program Cooperation under Grant KMUTNB-BasicR-64-17.

Conflicts of Interest: The authors declare no conflict of interest.

Appendix A. Laboratory Test Bench Description

The experimental setup of the DC microgrid platform is based on a ME²Power Fuel Cell System: 2.5 kW, 50 V, as shown in Figure A1. The 2.5 kW Methanol System includes a fuel reformer reactor that chemically transforms methanol fuel with water into hydrogen H₂ to both FC stacks. The proposed controller algorithm (see Figure 8) has been realized first through Matlab- Matlab/Simulink and then implemented into a dSPACE MicroLabBox. The sampling frequency was chosen at 25 kHz (=40 μ s of the sampling time), which corresponds to the switching frequency f_S (=25 kHz) of the FC converters. Besides, 1st order filters with a set cutoff frequency of 1 kHz (f_v) for voltage measurements (i.e., FC and DC bus)

and of 10 kHz (f_1) for current measurements (i.e., load and inductors) were used before the current and voltage measurements were injected into the control strategy through the dSPACE MicroLabBox. The implemented parameters of the FC converters are provided in Table A1 and the control parameters of the system are given in Table A2.

Table A1. Fuel cell converter parameters.

Symbol	Quantity	Nominal Value
v_C	Nominal DC Bus Voltage	110 V
v_{FC}	Nominal FC Voltage	50 V
$L = L_1 = L_2$	Inductances	200 μ H
$r = r_{L1} = r_{L2}$	Parasitic resistances	0.1 Ω
C_B	DC bus capacitance	500 μ F
f_s	Switching Frequency	25 kHz
$S_{11}, S_{12}, S_{21}, S_{22}$	Power MOSFET, IXFN90N85X	850 V, 90 A

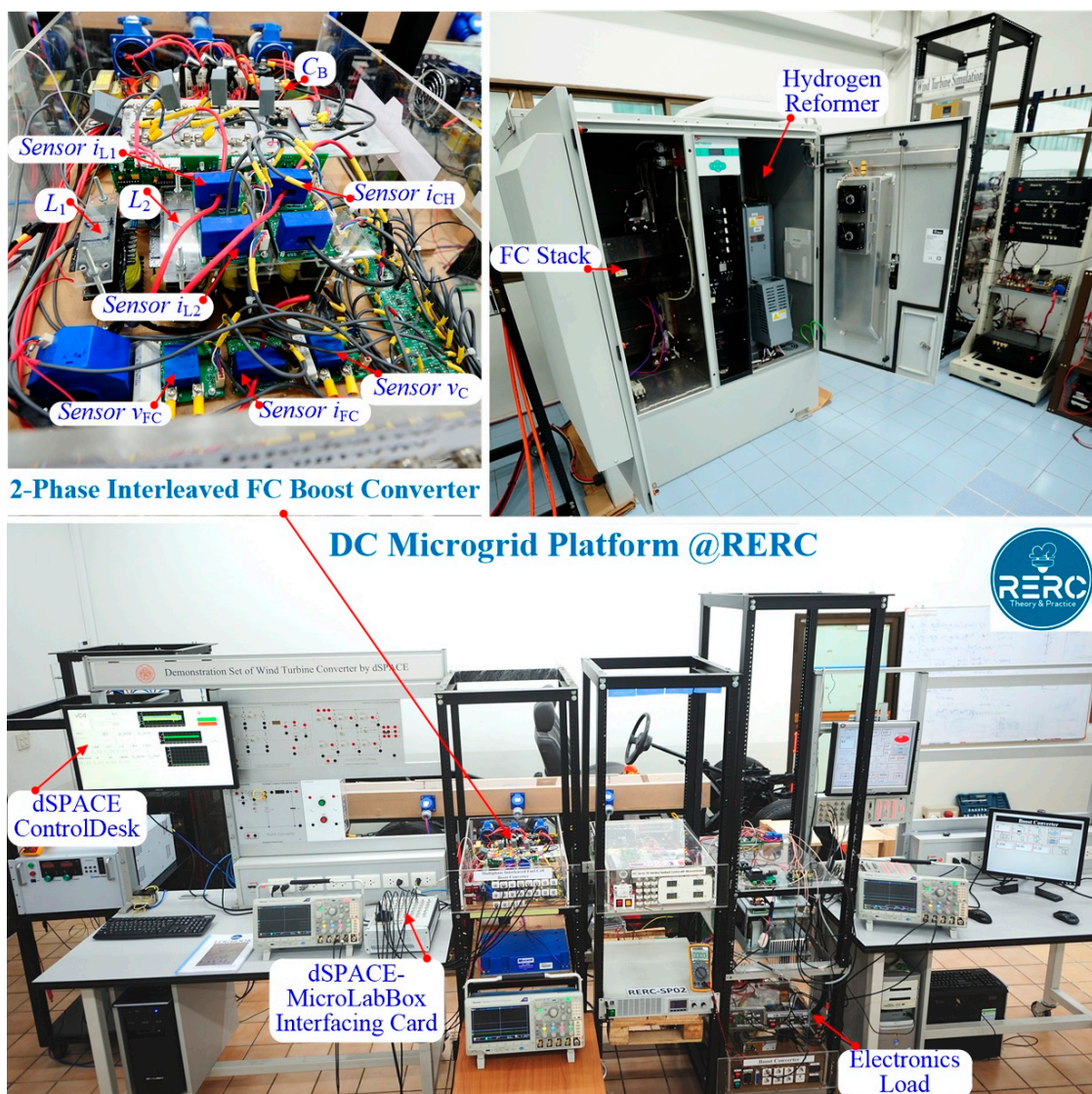


Figure A1. Overview of the DC microgrid platform realized in the laboratory (Renewable Energy Research Centre RERC, Bangkok, Thailand).

Table A2. Controller parameters.

Symbol	Quantity	Nominal Value
$v_{Cd} = (x_{3d})$	DC Bus Voltage Set-Point	110 V
$p_{FCRated}$	Nominal FC Power	2500 W
p_{FCmin}	Minimum FC Power	0 W
i_{LRated}	Nominal Inductor Current	25 A
i_{Lmin}	Minimum Inductor Current	0 A
K_R	Damping Gain	0.5
K_I	Integral Gain	150

References

1. Yao, G.; Du, C.; Ge, Q.; Jiang, H.; Wang, Y.; Ait-Ahmed, M.; Moreau, L. Traffic-Condition-Prediction-Based HMA-FIS Energy-Management Strategy for Fuel-Cell Electric Vehicles. *Energies* **2019**, *12*, 4426. [\[CrossRef\]](#)
2. Bizon, N.; Thounthong, P. Energy Efficiency and Fuel Economy of a Fuel Cell/Renewable Energy Sources Hybrid Power System with the Load-Following Control of the Fueling Regulators. *Mathematics* **2020**, *8*, 151. [\[CrossRef\]](#)
3. Bizon, N.; Mazare, A.; Ionescu, L.; Thounthong, P.; Kurt, E.; Oproescu, M.; Serban, G.; Lita, I. Better Fuel Economy by Optimizing Airflow of the Fuel Cell Hybrid Power Systems Using Fuel Flow-Based Load-Following Control. *Energies* **2019**, *12*, 2792. [\[CrossRef\]](#)
4. Guilbert, D.; N'Diaye, A.; Gaillard, A.; Djerdir, A. Reliability improvement of a floating interleaved DC/DC boost converter in a PV/fuel cell stand-alone power supply. *EPE J.* **2018**, *29*, 49–63. [\[CrossRef\]](#)
5. Guilbert, D.; N'Diaye, A.; Gaillard, A.; Djerdir, A. Fuel cell systems reliability and availability enhancement by developing a fast and efficient power switch open-circuit fault detection algorithm in interleaved DC/DC boost converter topologies. *Int. J. Hydrog. Energy* **2016**, *41*, 15505–15517. [\[CrossRef\]](#)
6. Mungporn, P.; Thounthong, P.; Sikkabut, S.; Yodwong, B.; Ekkaravaradome, C.; Kumam, P.; Junkhiaw, S.T.; Bizon, N.; Nahid-Mobarakkeh, B.; Pierfederici, S. Differential flatness-based control of current/voltage stabilization for a single-phase PFC with multiphase interleaved boost converters. In Proceedings of the 2017 IEEE European Conference on Electrical Engineering and Computer Science (EECS 2017), Bern, Switzerland, 17–19 November 2017; pp. 124–130. [\[CrossRef\]](#)
7. Vuyyuru, U.; Maiti, S.; Chakraborty, C.; Pal, B. A Series Voltage Regulator for the Radial DC Microgrid. *IEEE Trans. Sustain. Energy* **2019**, *10*, 127–136. [\[CrossRef\]](#)
8. Mohammadi, J.; Badrkhani Ajaei, F.; Stevens, G. Grounding the DC Microgrid. *IEEE Trans. Ind. Appl.* **2019**, *55*, 4490–4499. [\[CrossRef\]](#)
9. Mojica-Nava, E.; Rey, J.; Torres-Martinez, J.; Castilla, M. Decentralized Switched Current Control for DC Microgrids. *IEEE Trans. Ind. Electron.* **2019**, *66*, 1182–1191. [\[CrossRef\]](#)
10. Bhosale, R.; Agarwal, V. Fuzzy Logic Control of the Ultracapacitor Interface for Enhanced Transient Response and Voltage Stability of a DC Microgrid. *IEEE Trans. Ind. Appl.* **2019**, *55*, 712–720. [\[CrossRef\]](#)
11. Babaihgari, B.; Ullah, M.; Park, J. Coordinated control and dynamic optimization in DC microgrid systems. *Int. J. Electr. Power Energy Syst.* **2019**, *113*, 832–841. [\[CrossRef\]](#)
12. Siad, S.; Malkawi, A.; Damm, G.; Lopes, L.; Dol, L. Nonlinear control of a DC MicroGrid for the integration of distributed generation based on different time scales. *Int. J. Electr. Power Energy Syst.* **2019**, *111*, 93–100. [\[CrossRef\]](#)
13. Mardani, M.; Khooban, M.; Masoudian, A.; Dragicevic, T. Model Predictive Control of DC–DC Converters to Mitigate the Effects of Pulsed Power Loads in Naval DC Microgrids. *IEEE Trans. Ind. Electron.* **2019**, *66*, 5676–5685. [\[CrossRef\]](#)
14. Huangfu, Y.; Pang, S.; Nahid-Mobarakkeh, B.; Guo, L.; Rathore, A.; Gao, F. Stability Analysis and Active Stabilization of On-board DC Power Converter System with Input Filter. *IEEE Trans. Ind. Electron.* **2018**, *65*, 790–799. [\[CrossRef\]](#)
15. Hossain, E.; Perez, R.; Nasiri, A.; Bayindir, R. Stability improvement of microgrids in the presence of constant power loads. *Int. J. Electr. Power Energy Syst.* **2018**, *96*, 442–456. [\[CrossRef\]](#)

16. Dell'Isola, D.; Urbain, M.; Weber, M.; Pierfederici, S.; Meibody-Tabar, F. Optimal Design of a DC–DC Boost Converter in Load Transient Conditions, Including Control Strategy and Stability Constraint. *IEEE Trans. Transp. Electrification*. **2019**, *5*, 1214–1224. [[CrossRef](#)]
17. Thamm, W.; Nuchkrua, T.; Ruayariyasub, S. Sliding mode control for stabilizing DC-link of DC-DC converter in photovoltaic systems. In Proceedings of the 2nd International Symposium on Power Electronics for Distributed Generation Systems, Hefei, China, 16–18 June 2010. [[CrossRef](#)]
18. Li, K.; Boonto, S.; Nuchkrua, T. On-line Self Tuning of Contouring Control for High Accuracy Robot Manipulators under Various Operations. *Int. J. Control Autom. Syst.* **2020**, *18*, 1818–1828. [[CrossRef](#)]
19. Hussain, M.; Mishra, R.; Agarwal, V. A Frequency-Dependent Virtual Impedance for Voltage-Regulating Converters Feeding Constant Power Loads in a DC Microgrid. *IEEE Trans. Ind. Appl.* **2018**, *54*, 5630–5639. [[CrossRef](#)]
20. Namazi, M.; Nejad, S.; Tabesh, A.; Rashidi, A.; Liserre, M. Passivity-Based Control of Switched Reluctance-Based Wind System Supplying Constant Power Load. *IEEE Trans. Ind. Electron.* **2018**, *65*, 9550–9560. [[CrossRef](#)]
21. Kardan, M.; Asemanni, M.; Khayatian, A.; Vafamand, N.; Khooban, M.; Dragicevic, T.; Blaabjerg, F. Improved Stabilization of Nonlinear DC Microgrids: Cubature Kalman Filter Approach. *IEEE Trans. Ind. Appl.* **2018**, *54*, 5104–5112. [[CrossRef](#)]
22. He, W.; Soriano-Rangel, C.; Ortega, R.; Astolfi, A.; Mancilla-David, F.; Li, S. Energy shaping control for buck–boost converters with unknown constant power load. *Control Eng. Pract.* **2018**, *74*, 33–43. [[CrossRef](#)]
23. Thounthong, P.; Mungporn, P.; Guilbert, D.; Takorabet, N.; Pierfederici, S.; Nahid-Mobarakeh, B.; Hu, Y.; Bizon, N.; Huangfu, Y.; Kumam, P. Design and control of multiphase interleaved boost converters-based on differential flatness theory for PEM fuel cell multi-stack applications. *Int. J. Electr. Power Energy Syst.* **2020**, *124*, 106346. [[CrossRef](#)]
24. Zhang, M.; Borja, P.; Ortega, R.; Liu, Z.; Su, H. PID Passivity-Based Control of Port-Hamiltonian Systems. *IEEE Trans. Autom. Control* **2018**, *63*, 1032–1044. [[CrossRef](#)]
25. Pang, S.; Nahid-Mobarakeh, B.; Pierfederici, S.; Phattanasak, M.; Huangfu, Y.; Luo, G.; Gao, F. Interconnection and Damping Assignment Passivity-Based Control Applied to On-Board DC–DC Power Converter System Supplying Constant Power Load. *IEEE Trans. Ind. Appl.* **2019**, *55*, 6476–6485. [[CrossRef](#)]
26. Cupelli, M.; Gurumurthy, S.; Bhandari, S.; Yang, Z.; Joebges, P.; Monti, A.; De Doncker, R. Port Controlled Hamiltonian Modeling and IDA-PBC Control of Dual Active Bridge Converters for DC Microgrids. *IEEE Trans. Ind. Electron.* **2019**, *66*, 9065–9075. [[CrossRef](#)]
27. Zhou, P.; Yang, R.; Zhang, G.; Han, Y. Adaptive Robust Simultaneous Stabilization of Two Dynamic Positioning Vessels Based on a Port-Controlled Hamiltonian (PCH) Model. *Energies* **2019**, *12*, 3936. [[CrossRef](#)]
28. Meshram, R.; Bhagwat, M.; Khade, S.; Wagh, S.; Stankovic, A.; Singh, N. Port-Controlled Phasor Hamiltonian Modeling and IDA-PBC Control of Solid-State Transformer. *IEEE Trans. Control Syst. Technol.* **2019**, *27*, 161–174. [[CrossRef](#)]
29. Liu, X.; Liao, X. Fixed-Time H_∞ Control for Port-Controlled Hamiltonian Systems. *IEEE Trans. Autom. Control* **2019**, *64*, 2753–2765. [[CrossRef](#)]
30. Lei, Y.; Lin, X.; Zhu, Y. Passivity-Based Control Strategy for SMES under an Unbalanced Voltage Condition. *IEEE Access* **2018**, *6*, 28768–28776. [[CrossRef](#)]
31. Mungporn, P.; Thounthong, P.; Yodwong, B.; Ekkaravarodom, C.; Bilsalam, A.; Pierfederici, S.; Guilbert, D.; Nahid-Mobarakeh, B.; Bizon, N.; Shah, Z.; et al. Modeling and Control of Multiphase Interleaved Fuel-Cell Boost Converter Based on Hamiltonian Control Theory for Transportation Applications. *IEEE Trans. Transp. Electrification*. **2020**, *6*, 519–529. [[CrossRef](#)]
32. Yodwong, B.; Thounthong, P.; Guilbert, D.; Bizon, N. Differential Flatness-Based Cascade Energy/Current Control of Battery/Supercapacitor Hybrid Source for Modern e-Vehicle Applications. *Mathematics* **2020**, *8*, 704. [[CrossRef](#)]
33. Thounthong, P.; Rael, S.; Davat, B. Control Strategy of Fuel Cell and Supercapacitors Association for a Distributed Generation System. *IEEE Trans. Ind. Electron.* **2007**, *54*, 3225–3233. [[CrossRef](#)]
34. Van Verdeghe, J.; Lefebvre, M.; Kluyskens, V.; Dehez, B. Dynamical Modeling of Passively Levitated Electrodynamic Thrust Self-Bearing Machines. *IEEE Trans. Ind. Appl.* **2019**, *55*, 1447–1460. [[CrossRef](#)]
35. Thounthong, P.; Sikkabut, S.; Poonnoy, N.; Mungporn, P.; Yodwong, B.; Kumam, P.; Bizon, N.; Nahid-Mobarakeh, B.; Pierfederici, S. Nonlinear Differential Flatness-Based Speed/Torque Control with State-Observers of Permanent Magnet Synchronous Motor Drives. *IEEE Trans. Ind. Appl.* **2018**, *54*, 2874–2884. [[CrossRef](#)]

36. Sriprang, S.; Nahid-Mobarakeh, B.; Pierfederici, S.; Takorabet, N.; Bizon, N.; Kumam, P.; Mungporn, P.; Thounthong, P. Robust Flatness-based Control with State Observer-Based Parameter Estimation for PMSM Drive. In Proceedings of the 2018 IEEE International Conference on Electrical Systems for Aircraft, Railway, Ship Propulsion and Road Vehicles & International Transportation Electrification Conference (ESARS-ITEC), Nottingham, UK, 7–9 November 2018. [[CrossRef](#)]
37. Jiang, Y.; Xu, K. Model Order Reduction of Port-Hamiltonian Systems by Riemannian Modified Fletcher–Reeves Scheme. *IEEE Trans. Circuits Syst. II Express Briefs* **2019**, *66*, 1825–1829. [[CrossRef](#)]
38. Mungporn, P.; Khomfoi, S.; Kumam, P.; Shah, Z.; Burikham, P.; Kaewprapha, C.; Yodwong, B.; Thounthong, P.; Ekkaravarodome, C.; Bilsalam, A.; et al. Study of Hamiltonian Energy Control of Multiphase Interleaved Fuel Cell Boost Converter. In Proceedings of the 2019 Research, Invention, and Innovation Congress (RI2C), Bangkok, Thailand, 11–13 December 2019. [[CrossRef](#)]
39. Montoya, O.; Gil-Gonzalez, W.; Serra, F. PBC Approach for SMES Devices in Electric Distribution Networks. *IEEE Trans. Circuits Syst. II Express Briefs* **2018**, *65*, 2003–2007. [[CrossRef](#)]
40. Arias, A.; Ibarra, E.; Tranco, E.; Griñó, R.; Kortabarria, I.; Caum, J. Comprehensive high speed automotive SM-PMSM torque control stability analysis including novel control approach. *Int. J. Electr. Power Energy Syst.* **2019**, *109*, 423–433. [[CrossRef](#)]
41. Tu, H.; Feng, H.; Srdic, S.; Lukic, S. Extreme Fast Charging of Electric Vehicles: A Technology Overview. *IEEE Trans. Transp. Electrification* **2019**, *5*, 861–878. [[CrossRef](#)]
42. Li, Q.; Su, B.; Pu, Y.; Han, Y.; Wang, T.; Yin, L.; Chen, W. A State Machine Control Based on Equivalent Consumption Minimization for Fuel Cell/ Supercapacitor Hybrid Tramway. *IEEE Trans. Transp. Electrification* **2019**, *5*, 552–564. [[CrossRef](#)]
43. Di Noia, L.; Genduso, F.; Miceli, R.; Rizzo, R. Optimal Integration of Hybrid Supercapacitor and IPT System for a Free-Catenary Tramway. *IEEE Trans. Ind. Appl.* **2019**, *55*, 794–801. [[CrossRef](#)]
44. Yang, T.; Wang, L.; Wang, F.; Wei, A. Hybrid Predictive Control for a Current Source Converter in an Aircraft DC Microgrid. *Energies* **2019**, *12*, 4025. [[CrossRef](#)]
45. Benzaquen, J.; Fateh, F.; Shadmand, M.; Mirafzal, B. Performance Comparison of Active Rectifier Control Schemes in More Electric Aircraft Applications. *IEEE Trans. Transp. Electrification* **2019**, *5*, 1470–1479. [[CrossRef](#)]
46. Bosich, D.; Sulligoi, G.; Mocanu, E.; Gibescu, M. Medium Voltage DC Power Systems on Ships: An Offline Parameter Estimation for Tuning the Controllers’ Linearizing Function. *IEEE Trans. Energy Convers.* **2017**, *32*, 748–758. [[CrossRef](#)]
47. Boveri, A.; Silvestro, F.; Molinas, M.; Skjong, E. Optimal Sizing of Energy Storage Systems for Shipboard Applications. *IEEE Trans. Energy Convers.* **2019**, *34*, 801–811. [[CrossRef](#)]
48. Wu, Y.; Hu, K.; Sun, X. Modeling and Control Design for Quadrotors: A Controlled Hamiltonian Systems Approach. *IEEE Trans. Veh. Technol.* **2018**, *67*, 11365–11376. [[CrossRef](#)]
49. Montoya, O.; Garces, A.; Avila-Becerril, S.; Espinosa-Perez, G.; Serra, F. Stability Analysis of Single-Phase Low-Voltage AC Microgrids with Constant Power Terminals. *IEEE Trans. Circuits Syst. II Express Briefs* **2019**, *66*, 1212–1216. [[CrossRef](#)]
50. Sriprang, S.; Nahid-Mobarakeh, B.; Takorabet, N.; Pierfederici, S.; Bizon, N.; Kumam, P.; Thounthong, P. Permanent Magnet Synchronous Motor Dynamic Modeling with State Observer-based Parameter Estimation for AC Servomotor Drive Application. *Appl. Sci. Eng. Prog.* **2019**, *12*. [[CrossRef](#)]
51. Sriprang, S.; Nahid-Mobarakeh, B.; Takorabet, N.; Pierfederici, S.; Kumam, P.; Bizon, N.; Taghavi, N.; Vahedi, A.; Mungporn, P.; Thounthong, P. Design and control of permanent magnet assisted synchronous reluctance motor with copper loss minimization using MTPA. *J. Electr. Eng.* **2020**, *71*, 11–19. [[CrossRef](#)]

Publisher’s Note: MDPI stays neutral with regard to jurisdictional claims in published maps and institutional affiliations.



© 2020 by the authors. Licensee MDPI, Basel, Switzerland. This article is an open access article distributed under the terms and conditions of the Creative Commons Attribution (CC BY) license (<http://creativecommons.org/licenses/by/4.0/>).